Sublayer- and cell-type-specific neurodegenerative transcriptional trajectories in hippocampal sclerosis

Authors: Elena Cid[1]†, Angel Marquez-Galera[2]†, Manuel Valero[1], Beatriz Gal[1,3], Daniel C. Medeiros[1], Carmen M. Navarron[2], Luis Ballesteros-Esteban[1], Rita Reig-Viader[4,5], Aixa V. Morales[1], Ivan Fernandez-Lamo[1], Daniel Gomez-Dominguez[1], Masaaki Sato[6], Yasunori Hayashi[6,7], Alex Bayes[4,5], Angel Barco[2], Jose P Lopez-Atalaya[2,*], Liset M de la Prida[1,*]

Affiliations:

[1]Instituto Cajal, CSIC, 28002 Madrid, Spain.

[2]Instituto de Neurociencias, Universidad Miguel Hernández-Consejo Superior de Investigaciones Científicas (UMH-CSIC), 03550 Sant Joan d'Alacant, Alicante, Spain.

[3]Universidad Europea de Madrid, Villaviciosa de Odón, Madrid, Spain.

[4]Institut d'Investigació Biomèdica San Pau, 08041 Barcelona, Spain.

[5]Universitat Autònoma de Barcelona, 08193 Bellaterra, Cerdanyola del Vallès, Spain.

[6]RIKEN Brain Science Institute, Wako, Saitama, 351-0198, Japan.

[7]Department of Pharmacology, Kyoto University Graduate School of Medicine, Kyoto, 606-8501, Japan.

*** Co-corresponding authors:** jose.lopezatalaya@csic.es; lmprida@cajal.csic.es.

† These authors contributed equally to this work.

Abstract

Hippocampal sclerosis, the major neuropathological hallmark of temporal lobe epilepsy, is characterized by different patterns of neuronal loss. The mechanisms of cell-type specific vulnerability, their progression and histopathological classification remain controversial. Here using single-cell electrophysiology in vivo and immediate early gene expression, we reveal that superficial CA1 pyramidal neurons are overactive in epileptic rats and mice *in vivo*. Bulk tissue and single-nucleus expression profiling disclosed sublayer-specific transcriptomic signatures and robust microglial pro-inflammatory responses. Transcripts regulating neuronal processes such as voltage-channels, synaptic signalling and cell adhesion molecules were deregulated by epilepsy differently across sublayers, while neurodegenerative signatures primarily involved superficial cells. Pseudotime analysis of gene expression in single-nuclei and *in situ* validation revealed separated trajectories from health to epilepsy across cell types, and identified a subset of superficial cells undergoing a later stage in neurodegeneration. Our findings indicate sublayer- and cell type-specific changes associated with selective CA1 neuronal damage contributing to progression of hippocampal sclerosis.

Introduction

Epilepsies are brain disorders characterized by enduring predisposition to generate seizures with emotional and cognitive associated comorbidities. Despite significant therapeutic advances, one-third of patients remain resistant to pharmacotherapy (*1*). Temporal lobe epilepsy (TLE), the most prevalent form of pharmacoresistant epilepsy, is frequently associated with hippocampal sclerosis (*2*). Hippocampal sclerosis is characterized by specific patterns of neuronal loss affecting different hippocampal subfields from CA1 to CA3/4 areas, the hilus of the dentate gyrus and superficial layers of the entorhinal cortex (*3–5*). Factors such as epilepsy history, age of onset and relationship with early precipitating events may all influence the degree and severity of hippocampal sclerosis (*6*).

The most common form of hippocampal sclerosis (type 1; 60-80% TLE cases) shows severe neuronal loss of CA1, CA3 and CA4 pyramidal neurons and milder loss in CA2, with variability along the anteroposterior axis (*2*, *7*). Other cellular types, including microglia and astrocytes, are also affected (*2*, *8*). In contrast, type 2 hippocampal sclerosis (10-20% cases) is associated with predominant CA1 neurodegeneration and minimal loss in other regions (*2*). Given disparities between clinical series, there is no consensus yet on whether neuronal loss progresses or not along years (*5*, *6*). In addition, individual variabilities and anatomical inhomogeneities complicate classification (*9–11*). For instance, patchy neuronal loss has been described in the CA1 region in some cases, while in others it rather seems to adopt a more laminar profile (*12*). In some patients, cell loss concentrates in the CA4 region and the dentate gyrus, and is frequently integrated in dual pathologies, e.g. TLE and malformations of the cortical development, classified as type 3 hippocampal sclerosis (3-7%) (*13*). The mechanisms underlying specific vulnerability of diverse cells, their role in the histopathological landscape and clinical significance remain unknown.

Recent techniques and methods operating at single-cell resolution point to an exquisite cell-type specific organization that is instrumental for brain function (*14*, *15*). In the hippocampus, the CA1 region is organized radially in two distinct sublayers with characteristic gene expression gradients along the anteroposterior and proximodistal axes (*16–18*). Functionally, superficial (closer to radiatum) and deep (closer to oriens) CA1 pyramidal neurons project differentially and diverge in their participation of sharp-wave ripple activity, theta-gamma oscillations and behavioural-cognitive correlates (*19*, *20*). In spite of data suggesting critical regionalization of CA1 neuronal responses to ischemia, anoxia and epilepsy (*21–23*), little is known on their clinical relevance and potential relationship with neuronal vulnerability. Understanding the impact of cellular diversity and transcriptional changes in epilepsy progression may lend insights into more specific mechanisms towards new diagnostic and therapeutic opportunities.

Here, we combine gene expression profiling at the single-nucleus and microdissected tissue levels with single-cell electrophysiology to disclose epileptogenic and neurodegenerative changes running differentially across CA1 sublayers in an experimental model of hippocampal sclerosis. Our study highlights the importance of leveraging on cell type specificity to better understand the phenotypic complexities accompanying hippocampal sclerosis in epilepsy.

Results

Animals used in this study were examined in the chronic phase of the *status epilepticus* model of TLE (6-12 weeks post-*status*) when they already exhibited spontaneous seizures and interictal discharges (IID) (Sup.Fig.1A,B). In epileptic rats and mice, these events were typically associated with high-frequency oscillations (HFOs; Sup.Fig.1B), which are considered biomarkers of epileptogenesis (*23*, *24*). We focused in the dorsal hippocampus given the major role in associated cognitive comorbidities of epilepsy and more consistent neuronal loss as compared to ventral (*23*, *25*).

Large activity burden in superficial CA1 pyramidal cells during epileptiform activities

Single CA1 pyramidal cells were intracellularly recorded from chronic epileptic rats to evaluate their intrinsic excitability and activity during IID, sharp-wave (SPW) fast ripples and ictal discharges detected with multi-site silicon probes under urethane anesthesia (Fig.1A-D). Recorded cells were identified post hoc (with streptavidin) and immunostained against Calbindin, to classify them as deep (negative) or superficial pyramidal cells (positive) (Fig.1A). SPW-associated HFO events were automatically detected and classified as ripples (100-150 Hz), fast ripples (>150 Hz) and IID using amplitude and spectral information (Sup.Fig.1C, D), as before (*23*).

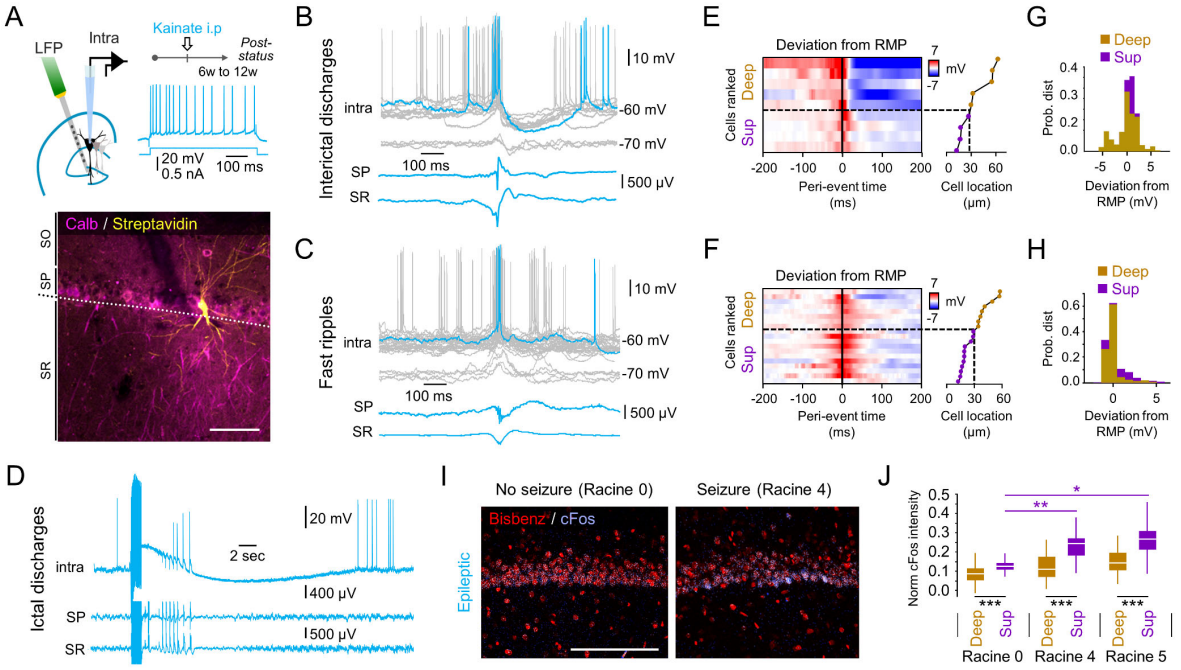

Figure 1

Fig.1. Differential responses of CA1 pyramidal cells during epileptiform activities. A, Intracellular and multi-site LFP recordings were obtained from urethane anesthetized epileptic rats. Cells were identified with streptavidin and tested against Calbindin. Scale bar 50 µm. **B**, Intracellular activity during IID at different membrane potentials (gray traces) in the representative cell shown in A. Traces are aligned by the peak of IID recorded at the stratum radiatum (SR). HFOs were recorded at the stratum pyramidale (SP). **C**, Responses of the cell shown in B during sharp-

wave fast ripples. **D**, Intracellular ictal discharges associated to a non-convulsive seizure evoked by electrical stimulation of Schaffer collaterals. **E**, Deviation from the resting membrane potential (RMP) recorded in individual cells during interictal discharges. Red colors reflect depolarization, blue hyperpolarization. Cells are ranked by their distance to SR and classified as deep and superficial (subplot at right). The discontinuous line marks sublayer limits. **F**, Same as in E for SPW-fast ripples. **G**, Mean membrane potential responses around IID events showed differences between deep and superficial cells (Friedman Chi2(1,333)=46.2049, p<0.001). Data from n=4 deep and n=5 superficial CA1 pyramidal cells. **H**, Same as in G for SPW-fast ripple events. Note larger after-event depolarization in superficial cells (Friedman Chi2(1,333)=14.67, p<0.0001). Data from n=8 deep and n=11 superficial CA1 pyramidal cells. **I**, c-Fos immunoreactivity detected 1h after sound stimulation in representative sections from one rat experiencing no seizure (Racine 0) and one rat exhibiting bilateral forelimb clonus with rearing (Racine 4). Scale 100 µm. **J**, Intensity of c-Fos from all pyramidal cells in one section per rat as a function of induced seizure severity (Racine scale). 2-way Friedman test effects for seizure severity (p<0.0001) and sublayer (p<0.0001). Posthoc mean rank differences ***, p<0.001. *, p<0.05; **, p<0.001.

Intracellular activities recorded during either IID events (n=9 cells; Fig.1B) and SPW-fast ripples (n=19 cells; Fig.1C) were typically associated with consistent depolarization from the resting membrane potential (RMP) and firing of all pyramidal cells examined (Fig.1E,F). A temporal analysis of membrane potential changes (30 ms bins) showed differences between cell types during both IID events (Fig.1G; Friedman Chi2(1,333)=3.88, p<0.001) and SPW-fast ripples (Fig.1H; Chi2(1,333)=14.67, p-value<0.0001), with superficial cells consistently showing larger depolarization. Post-event membrane potential responses recorded showed effect for the type of events (F(2,54)=5.95, p=0.0048), sublayer (F(1,54)=5.76, p=0.0202) and interaction (F(2,54)=4.74, p=0.0131). Post hoc Tuckey tests confirmed significant smaller hyperpolarization (p=0.0028; unpaired t-test) and higher firing rate (p=0.040) following IID events in superficial as compared with deep cells. We found some minor differences of intrinsic excitability between cell-types and groups (Sup.Table.1).

We reasoned that superficial pyramidal cells should be more steadily activated during seizures, given their poor post-event hyperpolarization. To evaluate this point we induced ictal discharges by repetitive 100 Hz stimulation (300 ms) of the contralateral CA3 region while recording from single cells. Cells recorded during ictal events exhibited variable long-lasting depolarizing shifts (3.8-13.5 sec; n=12 cells; Fig.1D) and only a minority were successfully recovered for histological validation (n=4 deep cells), preventing subsequent comparisons across sublayers. To circumvent this problem, we exposed 3 epileptic rats to high-pitched sounds to promote convulsive seizures (random pulses of 95-100 dB and 1-20 sec duration at 0.05-1 Hz during 10 min). Two rats experienced convulsive seizures with forelimb clonus and one rat remained unaffected, as judged by clinical criteria (Racine scale). Animals were sacrificed after 1 hour to evaluate expression of the immediate-early gene c-Fos as a function of seizure severity (Fig.1I). We noticed preferential expression of c-Fos in superficial pyramidal cells and significant effect of seizure severity (p<0.0001) and sublayer (p<0.0001; 2-way Friedman test) (Fig.1J).

Altogether, these results suggest higher responsiveness of superficial CA1 pyramidal cells during epileptiform activities in chronic epileptic rats.

Sublayer regionalization of epilepsy-associated transcriptional responses

To investigate how the differential responsiveness of deep and superficial cells may relate with distinct transcriptional responses across sublayers, we performed RNA sequencing (RNAseq) analysis of laser-microdissected samples from control (saline-injected) and epileptic rats (n=3 replicates each; Fig.2A; Suppl.Fig.2A,B). A public application provides easy visualization of these data (http://lopezatalayalab.in.umh-csic.es/CA1_Sublayers_&_Epilepsy/) (see also Sup.Table 2).

Analysis of LCM-RNAseq data revealed sublayer-specific genes common to control and epileptic animals (Fig.2B; deep versus superficial samples). Among these, we retrieved *bona fide* marker genes of superficial (*Calb1, Grm1,* and *Syt17*) and deep CA1 pyramidal cells (*Ndst4*), consistent with previous data in mice (*17*, *26*) (Suppl.Fig.2C; see Suppl.Fig.2D,E for validation by in situ hybridization). Sublayer gene expression analysis confirmed preserved regionalization in epileptic rats with only a subset of uncorrelated transcripts (Fig.2C; green dots; see Suppl.Fig.2F for less stringent criteria: Adj p-value<0.1). Strikingly, we found that some gene markers of other cell types, including interneurons (*Sst*, *Vip, Kit*), oligodendrocytes (*Mbp, Plp1, Mobp*) and microglia (*Csf1r*, *Tgfbr1*) exhibited sublayer differences, consistent with heterogeneous distribution of cell types across the CA1 radial axis (Fig.2B; Suppl.Fig.2E) (see next section).

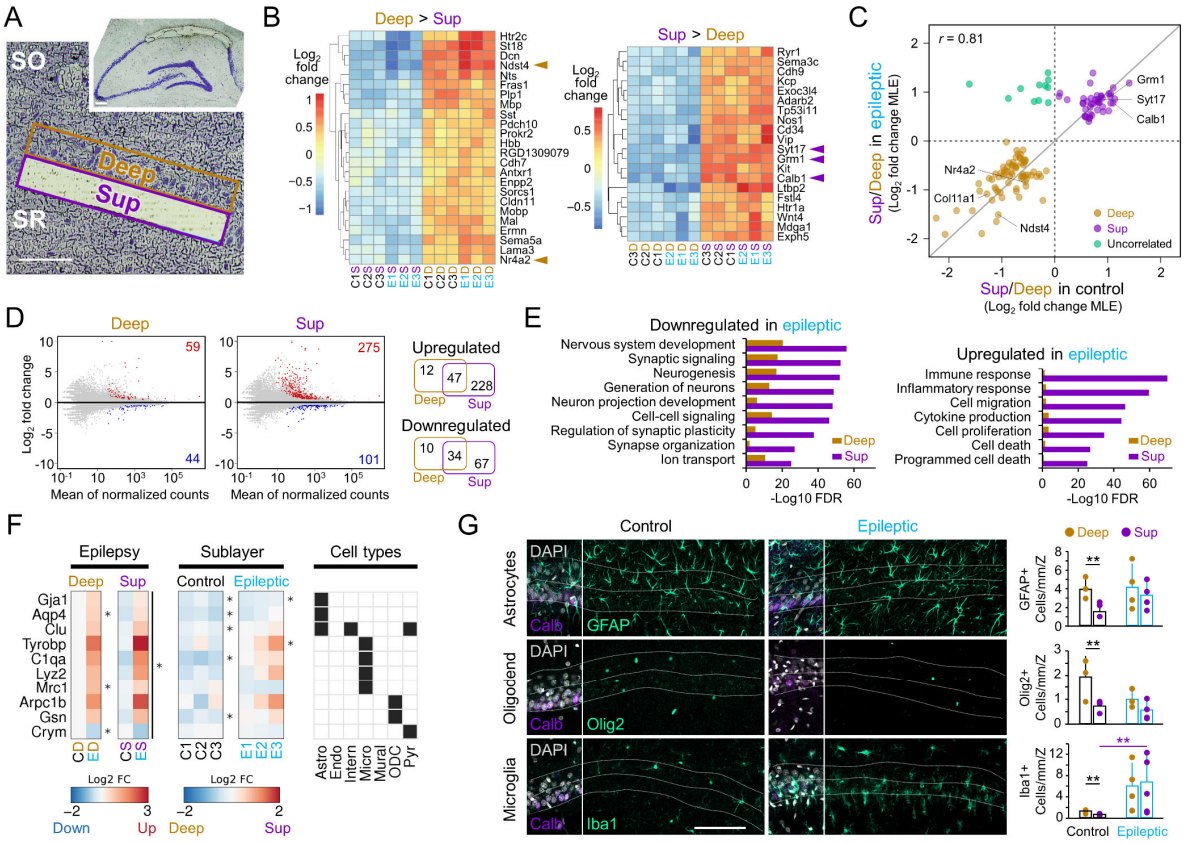

Figure 2

Fig.2. Bulk gene expression profiling of the epileptic hippocampal area CA1 reveals regionalized transcriptional responses. A, Representative LCM sampling of the superficial CA1 sublayer. Scale bar 100 µm. **B**, Heatmaps of genes differentially enriched in deep (D; left) and superficial CA1 sublayers (S; right) in three replicates from control (C) and epileptic (E) rats (Adj p-value<0.01 and LFC>0.5). Arrowheads point to *bona fide* gene markers of superficial (*Calb1, Grm1, Syt17*) and deep (*Ndst4*) pyramidal neurons. Note also the presence of gene markers for interneurons (e.g. *Vip, Sst, Sema3c, Kit*), and oligodendrocytes (*Plp1, Mbp, Mobp, Mal, Enpp2, Cldn11, Ermn*). **C**, Scatter plot of genes differentially expressed between superficial and deep CA1 sublayers in control or epileptic rats (Adj p-value<0.01). Note a subset of uncorrelated transcripts at the superficial sublayer in epileptic rats (green). MLE: maximum-likelihood estimate. **D**, MA plots showing epilepsy-associated DEGs in the deep and superficial sublayers (Adj p-value<0.01 and LFC>0.5). Venn diagrams at right show up- (red dots at left) and donwregulated DEGs (blue dots). **E**, GO analysis of upregulated and downregulated genes in the epileptic condition for deep and superficial sublayers (Adj p-value<0.01 and LFC>0.5). **F**, *Left*: Heatmaps showing mean differential expression (LFC) of cell markers genes in response to epilepsy (Epilepsy) in deep and superficial sublayers. *Middle*: Same as before but for sublayer effect (Sublayer) in control (Control) and epileptic (Epileptic) groups, shown as individual data. *Right:* Matrix shows cell types (Cell types) associated to each marker gene: Astro, astrocytes; Endo, endothelial cells; Intern, interneurons; Micro, microglia; Mural, mural cells; ODC, oligodendrocytes; Pyr, pyramidal cells. *, Adj p-value<0.1. **G**, *Left*: Representative control and epileptic sections immunostained against GFAP (Astrocytes; top), Olig2 (Oligodendrocytes; middle), and Iba1 (Microglia; bottom). The leftmost section on each row shows co-localization between the specific marker, Calb and DAPI. *Right*: Quantification of astrocyte (GFAP+), oligodendrocyte (Olig2+), and microglia (Iba1+) linear cell density across sublayers and groups. Significant differences of interaction between sublayer and groups for astrocytes ($F(1,5)=10.1$, $p=0.022$) and microglia ($F(1,5)=7.4$, $p=0.042$) with post hoc differences at deep-superficial layers in the control group. Effect of sublayer for oligodendrocytes ($F(1,5)=23.8$, $p=0.0045$. Differences between groups only for microglia cells. Data from n=3 control, n=4 epileptic rats. *, $p<0.05$; **, $p<0.01$ post hoc tests.

Next, we investigated the transcriptional changes associated to epilepsy across CA1 sublayers (control versus epileptic samples per sublayer). We identified 103 differentially expressed genes (DEGs) in the deep sublayer of control versus epileptic and 376 DEGs in the superficial sublayer (Fig.2D). While epilepsy-associated transcriptional changes run in similar direction in both sublayers (i.e. no counter-regulated genes), they were more exacerbated in the superficial CA1 (Fig.2D; Suppl.Fig.2H). Overall, we retrieved more upregulated than downregulated genes, particularly in the superficial (73% DEGs) versus the deep sublayer (57%) (Fig.2D; Venn diagrams at right). Functional enrichment analyses also revealed marked differences (Fig.2E). Downregulated DEGs typically involved Gene Ontology (GO) terms associated with neuronal processes, such as synaptic signaling, neuron projection development, regulation of synaptic plasticity, and synapse organization, including many well-known modulators of epileptogenic process such as *Cacna1a, Cntnap2, Kcnb1, Kcnip4, Gabbr2, Gria1, Grin2a and Nav2* amongst others (*27*) (Supp.Table.2). In contrast, significantly upregulated DEGs were more linked to immune and inflammatory responses, including cytokine production, cell migration, cell

207 proliferation, and programmed cell death (e.g. *Cx3cr1, P2ry12, Tgfb1, Itgb1, Ripk3*)
208 (Supp.Table.2). Most of these GO families were significantly enriched in the superficial CA1
209 sublayer (Fig.2E). Thus, differential gene expression analysis suggests that the nature and severity
210 of transcriptional responses to TLE may segregate radially across CA1.

211

212 ***Cell-type deconvolution of LCM-RNAseq data suggests sublayer-specific neurodegeneration***
213 ***associated to microglia***

214 Given sublayer heterogeneity of biological processes revealed by bulk LCM-RNAseq, we reasoned
215 that they might reflect different contribution by discrete cellular populations within the CA1 sample
216 and/or changes of cell-type composition in response to epilepsy.

217 To address this point, we leveraged on a published dataset of *bona fide* transcripts from 3,005
218 barcoded individual cells from the mouse somatosensory S1 cortex and CA1 regions (*14*),
219 (Suppl.Fig.3A). We performed unsupervised clustering to identify cell-type specific genes in LCM-
220 RNAseq data, which were grouped in seven major classes: pyramidal cells, interneurons, astrocytes,
221 mural and endothelial cells, microglia, and oligodendrocytes (Suppl.Fig.3B,C). In control animals,
222 signatures of all these cell types were prominent in the CA1 deep layer, while genes enriched in the
223 superficial sublayer were mostly associated to pyramidal neurons and interneurons
224 (Suppl.Fig.3D,E). In contrast, we noticed strong upregulation of gene markers for microglia (Micro;
225 e.g *Tyrobp*) and oligodendrocytes (ODC; e.g *Arpc1b*) at the superficial layers of the epileptic CA1
226 (Fig.2F). To evaluate this *in situ*, we performed immunofluorescence staining against protein
227 markers for microglia (Iba1), astrocytes (GFAP), and oligodendrocytes (Olig2) and quantified their
228 density across sublayers (Fig.2G, left). We confirmed the presence of a physiological segregation
229 of glial cell types across the CA1 sublayers (control) and changes in TLE, with between-groups
230 differences reaching significance for microglia (Fig.2G, right).

231 Prompted by these results, we dissected the contribution of microglia-associated transcripts in our
232 sample. We noticed that most of the uncorrelated transcripts in the comparison of sublayer-enriched
233 genes across conditions were highly expressed in microglia (green dots in Fig.2C and Suppl.Fig.2F;
234 see microglia-specific genes in Suppl.Fig.2G). Thus, we evaluated their potential functional effect
235 by building the microglial sensome (*28*), which was profoundly upregulated in the superficial
236 sublayer of epileptic rats (Suppl.Fig.4A). Moreover, evaluation of microglia-neuron interactions
237 via ligand-receptor pairing confirmed sublayer-specific effects (Suppl.Fig.4B). For example, in the
238 epileptic superficial CA1 subfield we found dysregulated expression of the transcript encoding the
239 CD200 receptor, whose expression in neurons provides a "don't eat me" signal that reduces
240 microglial activation (*29*). Similarly, *Cx3cl1*, a neuronal chemokine that dampens microglia
241 inflammatory response and neurotoxicity was also strongly downregulated whereas *C3* and *Csf1*
242 transcripts were upregulated in superficial CA1 sublayer (*30*, *31*). In contrast, the epileptic deep
243 CA1 sublayer showed a much weaker microglia signature and only *Cx3cl1* was found
244 downregulated (Supp.Fig.4B).

245 Our analyses reveal the heterogeneous distribution of resident cell types across the CA1 radial axis
246 of the normal hippocampus. Strikingly, we identified critical changes in the epileptic hippocampus,

247 including local accumulation of reactive microglia and changes of key modulators of the neuronal
248 immune response specifically at the superficial sublayer.

249

250 ***CA1 hippocampal sclerosis is degenerative and sublayer-specific***

251 Given the results described above, we sought to evaluate the anatomical landscape of CA1
252 hippocampal sclerosis. Previously, we reported significant reduction of linear cell density
253 concentrated at the CA1 region in the systemic kainate model of TLE in rats, more consistent with
254 sclerosis type 2 (*32*). To evaluate CA1 sublayers precisely, we combined immunostaining against
255 the CA1 marker Wfs1 with the superficial marker Calbindin (Fig.3A). Proximal, intermediate and
256 distal CA1 segments were evaluated separately in tissue from 10 control and 10 epileptic rats (1
257 section per animal, from -3.2 to -4.8 mm from bregma).

258 Cell loss in all three segments was mostly restricted to Calb+ superficial CA1 pyramidal cells in
259 chronic epileptic rats (Fig.3B; 3-way ANOVA for group, sublayer and proximo-distal effects all
260 significant at $p<0.0001$; post hoc Tukey test $p<0.001$). Since Calbindin immunoreactivity may be
261 affected during epileptogenesis (*33*), we exploited the transgenic mouse line Thy1.2-G-CaMP7-
262 DsRed2 with restricted expression on deep pyramidal cells (Fig.3C). We found similar
263 regionalization of neuronal loss at the intermediate and distal segments of chronic epileptic mice
264 using co-localization between DsRed2 and Wfs1 (Fig.3D, left; n=3 control, n=5 epileptic; 6-8
265 weeks post-*status*; significant interaction between group and sublayer $p=0.0006$; post hoc t-test
266 $p<0.01$). We also evaluated temporal trends of CA1 cell loss in epileptic rats where a time-
267 dependent decrease of Calb+ cells was appreciated ($r=-0.52$; $p=0.097$; Pearson correlation), but not
268 for control animals ($p=0.66$; Fig.3E) excluding age effects (*34*). We also examined sublayer-
269 specific vulnerability of CA1 neurons in the lithium-pilocarpine model in rats (*35*), which is more
270 consistent with type 1 hippocampal sclerosis (*32*). Notably, pilocarpine-treated rats showed similar
271 reduction of Calb+ CA1 pyramidal cells early along epileptogenesis ($p=0.0003$; n=5 rats; 3-6 weeks
272 post-*status*; Fig.3E, note full cell loss after 10 weeks post-*status*, arrowhead). Finally, to fully
273 exclude interaction with Calbindin immunoreactivity, we evaluated Wfs1+ cell density at deep and
274 superficial sublayers by relying only on anatomical criteria (location within sublayer) and found
275 consistent results in both TLE models (Fig.3F; 2-way ANOVA for group $p=0.005$).

276 To further confirm sublayer-specific neurodegeneration, we combined Fluoro-Jade staining, which
277 characteristically label degenerating cells, with Wfs1 immunostaining in sections from epileptic
278 rats at different time points after kainate (2-23 weeks; n=6 epileptic and n=2 saline-injected rats)
279 and again observed stronger neurodegeneration in superficial sublayers (Fig.3G; paired t-test
280 $p=0.0017$). Notably, double immunostaining against Calb and the microglial marker Iba1 revealed
281 an inversed correlation between the amount of microglia and the density of superficial pyramidal
282 neurons (Calb+; $r=-0.87$, $p=0.0236$), but not for deep cells (Calb-; Fig.3H). This result indicates
283 that loss of superficial pyramidal neurons is strongly associated to local accumulation of microglia.

Taken altogether, our results support the idea that hippocampal sclerosis results from specific interactions between different cell types in a particular niche (i.e. superficial CA1 pyramidal cells and activated microglia) leading to regionalized neurodegenerative signatures in the sclerotic CA1.

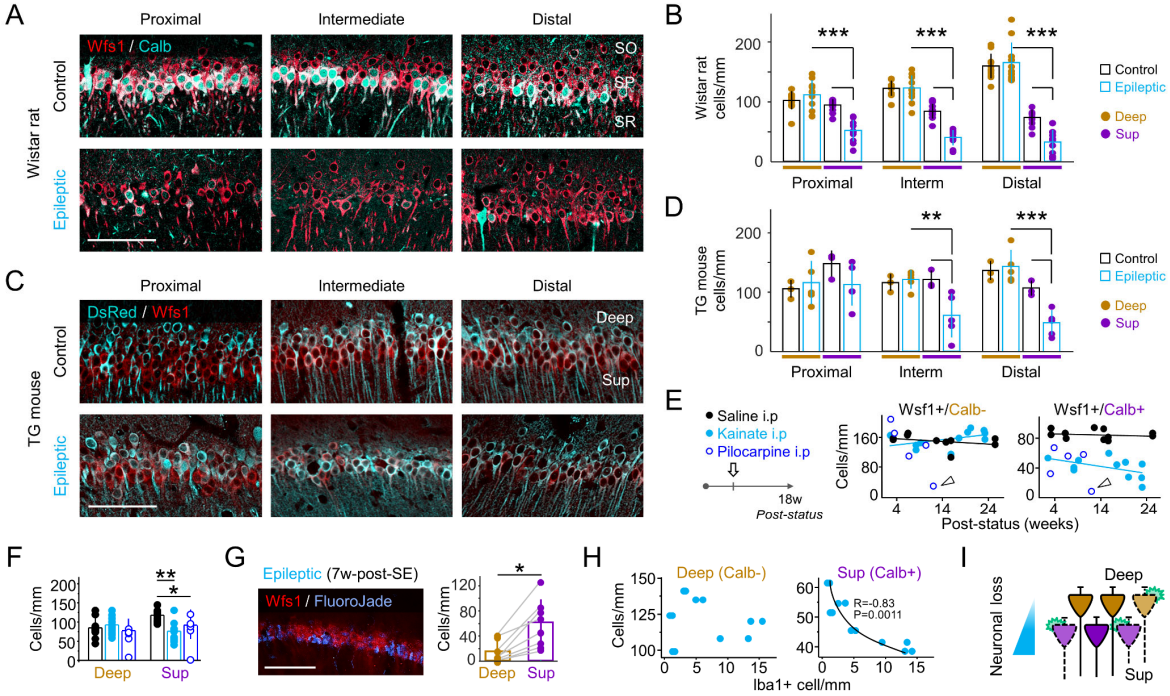

Figure 3

Fig.3. Hippocampal sclerosis is sublayer and cell-type specific. A, Immunostaining against the CA1 specific marker Wfs1 co-localized with Calb at proximal, intermediate and distal segments in control and epileptic rats. Scale bar, 100 µm. **B**, Quantification of CA1 linear cell density confirmed neuronal loss affecting mainly Calb+ cells. Data from n=10 control and n=10 kainate-treated epileptic rats (1 section per rat, -3.2 to -4.8 mm from bregma; 20x). Significant 3-way ANOVA for group ($F_{1,120}$=32.6, p<0.0001), proximodistal ($F_{2,120}$=11.7, p<0.0001) and sublayer ($F_{1,120}$=424,1; p<0.0001). Post hoc Tukey test: **, p<0.01; ***, p<0.005. **C**, Hippocampal sections from representative control and epileptic transgenic (TG) mouse expressing G-GaMP7-DsRed2 in Calb- deep pyramidal cells. **D**, Linear density data from n=3 control and n=5 epileptic TG mice (1 section per mouse at 20x). Significant 3-way ANOVA for groups ($F_{1,36}$=7.8, p=0.008) and sublayers ($F_{1,36}$=8.9, p=0.0051), no proximodistal effect. Post hoc t-test: **, p<0.01; ***, p<0.005. **E**, *Left*: Experimental timeline. *Right*: Mean density of Calb+ and Calb- CA1 pyramidal cells as a function of time. Data from n=10 control; n=10 epileptic rats (kainate) and n=5 epileptic rats (lithium-pilocarpine). Arrowheads point to a lithium-pilocarpine rat with full cell loss in CA1 10 weeks after status. **F**, CA1 mean cell loss in Wistar rats quantified as deep versus superficial. Superficial CA1 cells are more affected than deep cells. Significant effect for group in a 2-way ANOVA, $F_{2,48}$=5.9, p=0.005. Post hoc unpaired t-test *, p<0.01, **, p<0.01. **G**, Fluoro-Jade signal co-localized with Wfs1 and quantification of Fluoro-Jade+ cells across sublayers; n=8 Wistar rats. Paired t-test *, p<0.01. **H**, Density of deep (Calb-; left) and superficial (Calb+; right) pyramidal cells against the density of microglia (Iba1+) counted at deep and superficial sublayers

307 (data from n=6 epileptic rats). Significant correlation only for superficial. **I**, Schematic summary of
308 histopathological findings.

309

310 ***Single nucleus RNAseq confirms cell-type specific neurodegeneration of CA1 pyramidal cells***

311 To gain more insights into the transcriptional activity patterns underlying hippocampal sclerosis,
312 we performed unbiased high-throughput RNA sequencing of isolated single-nuclei (snRNAseq)
313 (Fig.4A). We analyzed the transcriptomes of 6,739 single high-quality CA1 barcoded nuclei
314 derived from 2 control and 2 epileptic mice (n=3,661 nuclei, >710 unique molecular identifiers or
315 UMI in control; n=3,078 nuclei, >540 UMI in epileptic samples). Consistent with recent reports
316 (*14*, *15*), barcoded cells were automatically classified in 13 clusters of CA1 nuclei that were then
317 aggregated in six major cell classes: excitatory neurons, interneurons, oligodendrocytes, microglia,
318 oligodendrocyte precursor cells and astrocytes (Suppl.Fig.5A,B; see Suppl.Fig5C for control versus
319 epileptic and Suppl.Fig5D for UMI levels and number of genes per cell type) (Supp.Table 3). Data
320 can be visualized in a public application (http://lopezatalayalab.in.umh-
321 csic.es/CA1_SingleNuclei_&_Epilepsy/).

322 We focused on pyramidal CA1 neurons, which represented 80% of cell population (5347 nuclei;
323 2,934 control and 2,413 epileptic). After two clustering rounds (Suppl.Fig.5E), we identified deep
324 and superficial pyramidal cells from control (1123 deep, 1810 sup) and epileptic samples (878 deep
325 and 1469 sup) and a small population of pyramidal nuclei that were mostly epilepsy-specific
326 (Pyr_ES, 67 nuclei: 66 from epileptic CA1; 1 from control CA1) (Fig.4B). Notably, clustering
327 exhibited consistent distribution of markers for deep (e.g. *Ndst4, Col11a1*) and superficial
328 pyramidal neurons (e.g. *Calb1, Epha3*) (Sup.Fig.5F,G). This specific population of Pyr_ES cells
329 showed total UMI values well above quality threshold (>500) and a number of annotated genes
330 lying within the control and epileptic ranges (Suppl.Fig.5H), excluding potential artifacts.
331 Differential expression analysis of Pyr_ES cells against all detected cells excluding deep and
332 superficial pyramidal neurons, revealed enrichment of pyramidal CA1 marker genes such as *Gria2*,
333 *Rasgrf1*, *Camkv* and *Brd9*, along with other transcripts enriched in excitatory neurons including
334 *Hs6st3*, *Cntnap2*, *Kcnh7*, *Kcnip4*, *and Meg3*, which confirmed their pyramidal nature
335 (Suppl.Fig.5I,J). Similar to our LCM-RNAseq observations at the tissue level, we found consistent
336 correlation of sublayer-specific genes in control and epileptic samples (Fig.4D; Suppl.Fig.6).

337 First, we sought to identify gene programs underlying the differential vulnerability of deep and
338 superficial CA1 pyramidal cell in response to epilepsy (Adj p-value<0.05). DEGs common to both
339 cell-types were associated with the modulation of synaptic transmission, synapse organization and
340 regulation of membrane potential (Fig.4E,F; common genes in black). Single-nucleus differential
341 expression analysis also revealed striking differences between superficial and deep cells in genes
342 involved in synaptic signaling and ion membrane transport (Fig.4E,F). To exclude effects of
343 different sample size between groups and cell-types, we evaluated the top-ranked 300 DEGs and
344 found similar GO families differentially involved (Suppl.Fig.7A). These include the gamma-
345 aminobutyric acid (GABA) signaling pathway, calcium ion transport, potassium ion transport,
346 regulation of glutamatergic synaptic transmission, axon growth and guidance and synapse
347 assembly. Notably, we also noted cell-type specific changes in genes related to neuronal survival.
348 For instance, we found significant upregulation of the death associated protein kinase 1 (*Dapk1*)

specifically in superficial CA1 neurons (*36*) (Fig.4G). Conversely, genes associated to pro-survival receptors TrkB (*Ntrk2*), TrkC (*Ntrk3*), and the sortilin-related VPS10 domain containing receptor 3 (*Sorcs3*) were exclusively upregulated in deep cells (*37*, *38*) (Fig.4G). Other genes regulating neuronal vulnerability to insults were found deregulated in both populations of CA1 pyramidal neurons. These include the anti-apoptotic genes *Akt3*, *Chl1* and *Spag5*, and the pro-apoptotic gene *Nkain2* (*39–41*) (Fig.4G).

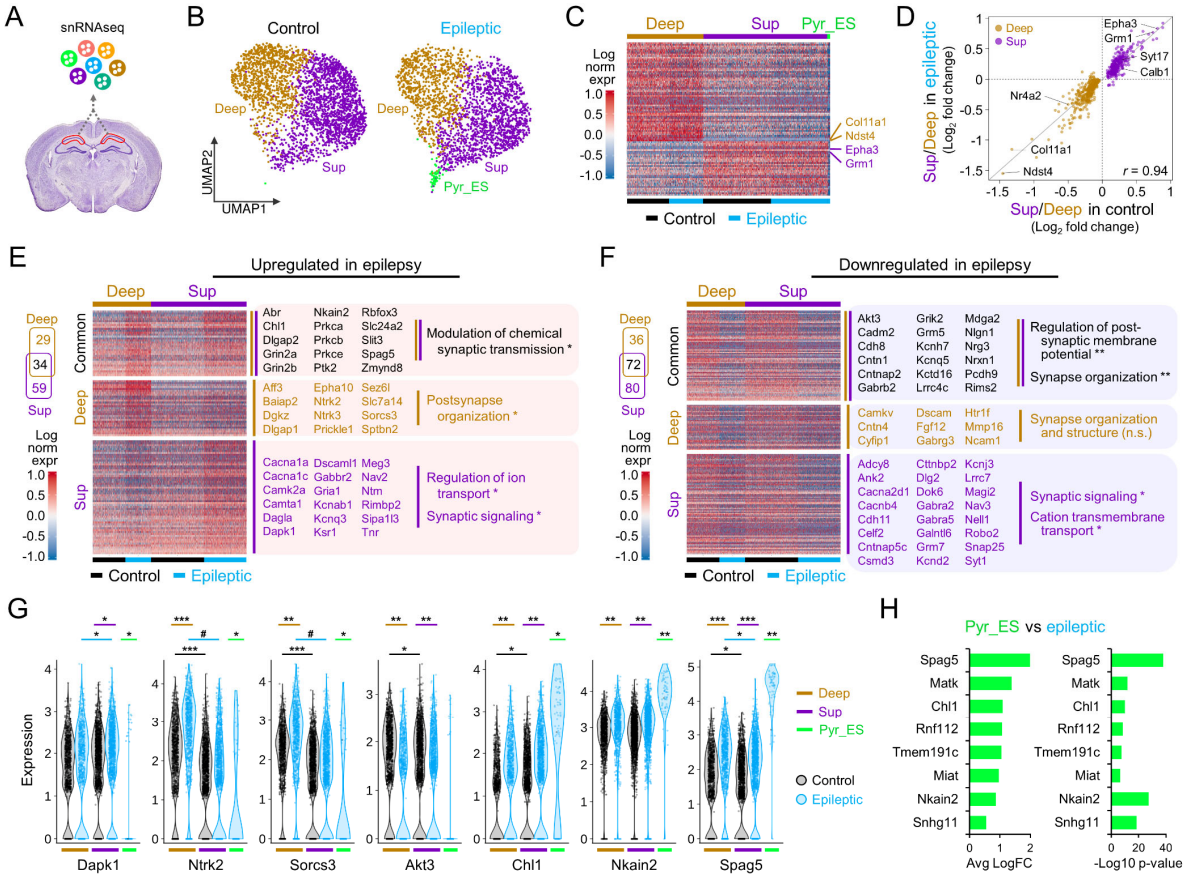

Figure 4

Fig.4. Single nucleus RNAseq profiling of the normal and epileptic CA1 area. A, Experimental schema of intact nuclei isolation and massive parallel droplet encapsulation for single-nucleus transcriptional profiling. Nuclei were isolated from CA1 region of adult mice and purified by flow cytometry for single nucleus RNAseq (snRNAseq). **B**, UMAP plots of CA1 pyramidal neuronal subtypes segregated by condition (control and epileptic). Pyr_ES: epilepsy-specific. **C**, Heatmap showing normalized expression (normalized log transformed UMIs) for principal gene markers for deep (Deep), superficial (Sup) neurons in control and epileptic mice (96 enriched genes: 62 deep, 34 sup; absolute LFC>0.25; min. pct>0.5; Adj p-value<1e-30). Note the presence of a subset of cells with differential gene expression corresponding to the epilepsy-specific cell population (Pyr_ES, green). **D**, Scatter plot showing significantly enriched genes in superficial and deep CA1 neurons in control mice and their relative level of enrichment in epileptic animals (Adj p-value<0.05; 493 genes). Gene expression levels of CA1 neuronal subtype-specific enriched genes are preserved in epilepsy. **E**, Venn diagram and heatmap of DEGs upregulated by epilepsy (Adj p-

368 value<0.05, Wilcoxon rank sum test). Heatmap shows normalized expression levels (normalized
369 log transformed UMIs) for upregulated DEGs that are common (34 genes) or specific to deep (29
370 genes) and superficial (59 genes) CA1 neurons. Representative genes and significant GO terms
371 associated to each gene list are highlighted at right. *FDR p<0.05 (Fisher's exact test). **F**, Same for
372 downregulated genes. **G**, Violin plots showing normalized expression value (normalized log
373 transformed UMIs) of selected genes in deep and superficial neurons in epilepsy (blue) and control
374 (black). Wilcoxon rank sum test *p<0.05; **p<1E-10; ***p<1E-50; #p<1E-100. Expression levels
375 in Pyr_ES cells is also shown (green). **H**, Bar chart of fold change (left) and significance (right) for
376 most upregulated genes in Pyr_ES when compared with epileptic CA1 pyramidal cells (absolute
377 fold change >0.5 and transcript detection in >50% of the nuclei).

378

379 We next focused on the small cluster of epilepsy-specific Pyr_ES cells (Fig.4B, green). When
380 compared against control pyramidal cells, Pyr_ES cells showed transcriptional dysregulation of the
381 GO families that were altered in superficial and deep CA1 neurons in epilepsy (Suppl.Fig.7B). To
382 avoid confounding effects caused by the small sample size, we focused in those transcripts
383 identified as differentially expressed between Pyr_ES and all other epileptic cells, that were well
384 represented in both populations (i.e. detected in at least 50% cells per group; min. pct1>0.5 and
385 min. pct2>0.5). Notably, many of these transcripts were upregulated more largely in Pyr_ES
386 neurons as compared to other epileptic cells, including the previously mentioned apoptotic-related
387 genes *Spag5*, *Chl1* and *NKain2* (Fig.4H; Suppl.Fig.7B,C).

388 Therefore, our analysis confirmed profound transcriptional changes related to neuronal excitability
389 and neurodegeneration in epileptic CA1 pyramidal neurons. Notably, these functions appear to be
390 segregated across deep and superficial cell-types consistent with electrophysiological, LCM-
391 RNAseq and histological data. Notably, snRNAseq analysis revealed disease-associated genes that
392 were highly cell-type specific, including some with key functions in neuronal survival. Hence,
393 epileptic-induced cell-type-specific regulation of genes with key roles in synaptic plasticity and
394 survival is a potential molecular link between differential activity burden and vulnerability across
395 CA1 radial axis leading to regionalized hippocampal sclerosis.

396

397 ***Pseudotemporal ordering reveals sublayer-specific neurodegenerative progression***

398 Based on data above we speculated that epilepsy-related responses and degenerative signals might
399 evolve distinctly across cell-types and sublayers. This may be especially critical for cell death
400 programs accompanying hippocampal sclerosis. To glean insights into these transitional states, we
401 used manifold learning leveraged in nearest-neighbor information to automatically organize cells
402 in trajectories along a principal tree reflecting progression of associated biological processes (*42*).

403 Low dimensional embedding of the automatically learnt underlying trajectory produced a spanning
404 tree revealing a topological structure with four main branches (A, B, D, E) and two bifurcation
405 points (1, 2; Fig.5A). Most nuclei at branches A and B were from cells identified as deep, whereas
406 branches D and E were populated mostly by superficial cells (Fig.5B). Interestingly, control and
407 epileptic cells distributed differently. Branches A and D were mostly populated by control
408 pyramidal cells, whereas branches B and E contained the vast majority of epileptic cells (Fig.5C,D).

The trajectory topology suggested that the transcriptional state of single cells progress along sublayer-specific disease trajectories from a basal state (branches A, D) to the epileptic condition (branches B, E) (Fig.5C). Notably, epilepsy-specific Pyr_ES cells were retrieved at the end of the superficial epileptic E path, suggesting that epileptic Pyr_ES cells may be superficial neurons at a terminal pathological state (Fig.5B; green arrowhead).

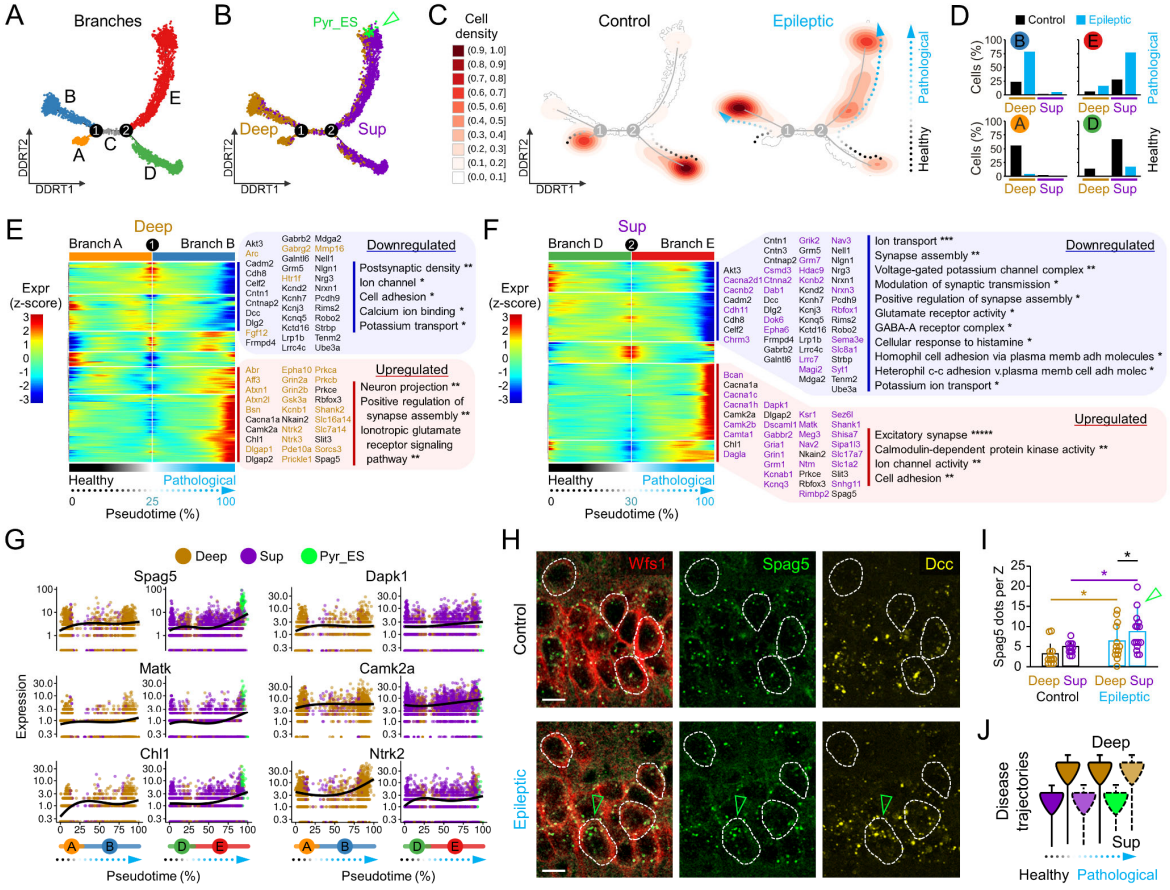

Figure 5

Fig.5. Pseudotemporal ordering of transcriptional changes unfolds separate disease trajectories across CA1 sublayers. A, UMAP plot of pseudotemporal trajectory analysis of pyramidal cells subpopulations along DDRTree coordinates uncovers four major branches (A,B,D,E) and segregated from two branching points (1,2). **B**, Same plot as in A showing distribution of pyramidal cells subpopulations (deep, superficial, Pyr_ES) across pseudotime trajectories. Arrowhead points to Pyr_ES cells located at the endpoint of branch E. **C**, Heatmap showing distribution of pyramidal cells subpopulations across pseudotime trajectories by condition (control and epileptic). **D**, Distribution of pyramidal cell subtypes across the trajectory topology. **E**, Heatmap of top-ranked 250 branched expression analysis modeling (BEAM) significant changes through the progression across the trajectory from branch A (basal state) to B (epilepsy) (deep cells). Note deep-specific expression up- (red) and down-regulation (blue) kinetics of the transcripts from the basal healthy state to the epileptic state. **F**, Same for the superficial-specific trajectory from basal state (branch D) to the epileptic condition (branch E). **G**, Examples of gradient progression across disease trajectory for significantly modulated genes in epilepsy related to

428 neuronal survival (*Spag5*, *Matk*, *Chl1*, *Dapk1*, *Camk2a*, and *Ntrk2*). **H**, Immunostaining against the
429 CA1 pyramidal cell marker Wfs1 and multiplexed RNAscope for *Spag5* and *Dcc* transcripts. Cells
430 with their soma in the confocal plane are outlined. Note significant accumulation of *Spag5* in an
431 epileptic cell (green arrowhead). **I**, Quantification of *Spag5* in deep and superficial CA1 neurons in
432 3 control and 3 epileptic mice, as counted in one confocal plane per animal (2-way ANOVA effect
433 for group F(1,51)=4.225, p=0.0450 and sublayers F(1,51)=11.521, p=0.0013; *, p<0.05 posthoc t-
434 test). Data from 27 control (14 deep, 14 superficial) and 28 epileptic cells (15 deep, 13 superficial).
435 Green arrowhead indicates cells with high *Spag5* expression. **J**, Schematic summary of disease
436 trajectories reflecting pseudotime progression from control to epilepsy.

437

438 To identify mechanisms underlying single-cell transcriptional changes from health to disease we
439 performed quantitative comparison of gene expression kinetics across trajectories in each cellular
440 population (DDRTree method) (*43*). By comparing the top-ranked 250 DEGs in deep (max FDR =
441 8.94E-4; likelihood ratio test) versus superficial cells (max FDR=5.8E-19), we found about 50% of
442 genes (124 genes) associated to epilepsy carrying significant cell-type specific trajectories.
443 Consistent with our previous results, we found that genes deregulated in epilepsy in superficial CA1
444 neurons show tight functional association among them, leading to high proportion of significantly
445 enriched ontology terms as compared to genes deregulated in deep CA1 neurons (Fig.5E,F). Again,
446 significantly enriched ontology terms were related to structural and functional neuronal plasticity.
447 Interestingly, pseudotemporal kinetics also revealed marked differences in the progression across
448 sublayers of genes with important functions in regulating neuronal survival. For instance, gene
449 transcript levels of the death associated protein kinase 1 (*Dapk1*) showed robust increase in
450 superficial epileptic cells, whereas gene expression levels of the pro-survival receptors TrkB
451 (*Ntrk2*) and TrkB (*Ntrk3*) along with other genes playing key functions in neurons such as *Sorcs3*
452 and *Aff3* were upregulated specifically in deep pyramidal cells (Fig5G, Sup.Fig.7D; Sup.Table3).
453 Other genes also related to neuronal vulnerability such as *Camk2a* and *Nrg3* displayed similar
454 changes along disease trajectory in both cell types. Strikingly, the subset of apoptotic-related genes
455 *Spag5, Matk* and *Chl1* reached their maximal expression level in Pyr_ES at the end of the
456 transcriptional trajectory in superficial cells (Fig.5G, green).

457 To confirm these trends *in situ* we combined the single-molecule amplification method RNAscope
458 with immunostaining against the CA1 pyramidal cell marker Wfs1 in coronal brain sections of
459 control and epileptic mice (Fig.5H; Sup.Fig.7E). For RNAscope we selected *Spag5,* which
460 exhibited the largest changes in epilepsy (Fig.5G; see Fig.4H), and the superficial gene marker *Dcc*
461 which is not affected by epilepsy (Supp.Fig.6A; Supp.Fig.7F-H). We found different distribution
462 of *Spag5* dots in sections from control and epileptic mice with significant effects for groups (2-way
463 ANOVA F(1,51)=4.225, p=0.0450) and sublayers (F(1,51)=11.521, p=0.0013; no interaction, all
464 cells counted in one confocal section per animal; 3 control, 3 epileptic) (Fig.5I). Consistent with
465 trajectory analysis, a small subset of pyramidal cells exhibited large levels of Spag5 dots roughly
466 resembling expression distribution from snRNAseq data (Fig.5H, green arrowhead; see distribution
467 in Fig.4G), giving support to the idea that these cells represent a later stage in neurodegeneration
468 (Fig.5J).

469

470 **Discussion**

471 Our work identifies sublayer-specific transcriptional changes in experimental hippocampal
472 sclerosis. Using a combination of techniques, we found that acquired TLE involves heterogeneous
473 biological processes running across deep and superficial CA1 pyramidal cells. Our data suggest
474 that epileptogenesis and the accompanying hippocampal sclerosis are evolving processes that affect
475 the transcriptional state of neurons in a cell-type specific manner.

476 Hippocampal sclerosis is a heterogeneous histopathological entity (*2*). The prognosis value of
477 certain subtypes has been largely debated but emerging data suggest it deserves further
478 consideration in light of cell-type specificity (*12*). Superficial and deep CA1 pyramidal cells are
479 differently innervated by local circuit GABAergic interneurons, express different neuromodulatory
480 receptors, project differentially to cortical and subcortical regions and participate distinctly of
481 hippocampal oscillations (*17*, *19*, *20*). The more sustained excitability of superficial pyramidal cells
482 (in terms of post-event depolarization and increased firing rate) and their consistent stronger
483 expression of the immediate-early gene associated protein c-Fos after individual seizures, suggest
484 they undergo larger activity burden as compared with deep cells (Fig.1). While our snRNAseq
485 analysis identified many transcripts differentially regulated between deep and superficial CA1
486 neurons that may underlie pro-epileptogenic changes in intrinsic excitability, microcircuit
487 mechanisms are key contributors to these differences. First, perisomatic inhibition by parvalbumin
488 (PV) basket cells is remarkably higher in deep than superficial cells (*20*, *44*). Second, superficial
489 cells are more likely to be driven by presynaptic CA3 activity than deep cells (*44*). Similarly, direct
490 inputs from layer III pyramidal neurons in the medial entorhinal cortex are biased by deep CA1
491 cells, whereas projections from the lateral entorhinal cortex are stronger in superficial (*45*). Given
492 loss of medial layer III inputs and sprouting of lateral inputs together with specific cannabinoid
493 type-1 receptors pathways (*46*, *47*), it is very much likely all these changes contribute to more
494 sustained activation of superficial cells.

495 Transcriptional dysregulation is a central feature of most neurodegenerative diseases. Our
496 transcriptional profiling in laser-microdisected CA1 deep and superficial sublayers (LCM-
497 RNAseq) revealed strong regionalized responses to acquired epilepsy. We found significantly
498 larger transcriptional changes of GO terms associated with the immune and inflammatory
499 processes, cytokine production and programmed cell death in the superficial sublayer (Fig.2). This
500 includes *Cx3cr1*, *P2ry12* and *Il18* amongst others previously described genes to play major roles
501 in microglial activation and neurodegeneration associated to epilepsy (*48–50*). For deep pyramidal
502 sublayers transcriptional changes were milder in general and mostly involved deregulation of genes
503 associated with changes of excitability, homeostatic regulation and synaptic signalling, such as
504 *Kcnq2, Kcnq5*, *Cntnap2*, and *Gabrb2* (*51–53*). Many of these changes were confirmed with
505 snRNAseq analysis (Fig.4), which disclosed significant upregulation of the death associated protein
506 kinase 1 (*Dapk1*) specifically in superficial CA1 neurons (*36*) while genes associated to pro-
507 survival receptors TrkB (*Ntrk2*), TrkC (*Ntrk3*), and the sortilin-related VPS10 domain containing
508 receptor 3 (*Sorcs3*) were mostly upregulated in deep cells (*37*, *38*).

509 By leveraging on unsupervised branched expression learning, we identified deviating
510 transcriptional disease trajectories in deep and superficial pyramidal cells (Fig.5). Some of the GO
511 terms involved suggest that transition from the normal to the epileptic condition in deep cells is

512 more likely associated to changes of synaptic signalling and excitability (i.e. they reflect
513 microcircuit alterations), whereas superficial cells rather move differentially along transcriptional
514 changes impacting on cell-cell communication (i.e. neuron-microglia interactions). Such different
515 latent trends might actually suggest that deep and superficial cells are at different stages in the
516 neurodegenerative process or being affected by pathways leading to differential vulnerability. For
517 instance, while we found deregulated expression of genes associated with apoptotic pathways that
518 were common to both cell types in response to epilepsy (i.e. *Akt3, Nrg3 and Camk2a*) (*39*, *41*, *54–*
519 *56*), genes related to cell death were found deregulated specifically in superficial or deep neurons.
520 In superficial cells, epilepsy resulted in decreased expression of brain derived neurotrophic factor
521 (*Bdnf*), and increased transcript levels of pro-apoptotic pathway activator Death-associated protein
522 kinase 1 (*Dapk1*) (*36*). Conversely, in deep pyramidal neurons, epilepsy led to robust increase in
523 the expression of the gene encoding the pro-survival receptors TrkB (*Ntrk2*) and TrkC (*Ntrk3*)(*37*,
524 *38*). Interestingly, pseudotime analysis mapped fewer control cells along the epileptic branches in
525 both sublayers suggesting that latent sublayer specific transcriptional processes might actually be
526 running along life (*57*).

527 Our snRNAseq analysis also disclosed an epilepsy-specific pyramidal cell population, Pyr_ES,
528 which accumulated at the end of the superficial trajectory branch (Fig.5B, arrowhead). This subset
529 of pyramidal cells displayed remarkable expression of neurodegeneration related transcripts such
530 as *Cdk5, Ckb, Matk, Chl1, and Spag5* (*58*). The presence of cells with very high number of *Spag5*
531 molecules in the superficial sublayer of the epileptic CA1 was confirmed by combined
532 immunofluorescence and single-molecule amplification methods. Thus, our results indicate that
533 genes more largely dysregulated in epilepsy are specifically expressed by vulnerable subset of
534 pyramidal neurons undergoing later stages of neurodegeneration by the time of sampling. We
535 propose that Pyr_ES cells reflect the accumulated pro-epileptic transitional changes leading to
536 epileptogenesis and neurodegeneration, as suggested by their extreme location along disease
537 trajectories.

538 Altogether, our results identify previously unobserved heterogeneity in the neuronal patterns of
539 activity of deep and superficial CA1 pyramidal neurons in epilepsy, discover specific gene expression
540 signatures across CA1 deep-superficial sublayers that are associated to neuronal loss and hippocampal
541 sclerosis, reveal disease trajectories of deep and superficial CA1 pyramidal neurons in epilepsy, and
542 uncover the underlying transcriptional programs. By dissecting the transcriptional landscape across
543 CA1 sublayers in epilepsy, our work offers new insights into the mechanisms regulating
544 epileptogenesis and highlights the importance of leveraging on cell type specificity to better
545 understand the phenotypic complexities accompanying hippocampal sclerosis in epilepsy.
546

547 **Materials and Methods**

548 All experimental protocols and procedures were performed according to the Spanish legislation
549 (R.D. 1201/2005 and L.32/2007), the European Communities Council Directives of 1986
550 (86/609/EEC) and 2003 (2003/65/CE) for animal research, and were approved by the Ethics
551 Committee of the Instituto Cajal.

552

553 *Epilepsy model*

554 Adult male Wistar rats (180–200 g), as well as wild-type C57 and transgenic mice (20-25 g), were
555 treated with multiple intraperitoneal injections of kainate (5 mg/kg) at hourly intervals until they
556 reached *status* epilepticus. Transgenic mouse lines included the Thy1.2-G-CaMP7-DsRed2
557 (c57BL/6J-Tg(Thy1-G-CaMP7-DsRed2)492Bsi, stock RBRCO6579, RIKEN), the Calb1-Cre
558 (Jackson Lab, stock No:023531; Calb1-2A-dgCre-D) and the Calb1-Cre line crossed with the
559 tdTomato reporter line (Jackson Lab, stock No:007905; Ai9). The *status* was defined as a condition
560 of continuous seizures lasting longer than 30 min. In a subset of rats, the lithium-pilocarpine model
561 was used. These rats were i.p. injected with pilocarpine hydrochloride 12–24 hr after the injection
562 of lithium chloride (127 mg/kg, i.p.). Between one and four doses of 10 mg/kg pilocarpine were
563 injected every 30 min until the *status* epilepticus was reached. Diazepam (4 mg/kg) was injected 1
564 h post-*status* to stop convulsions in all animals. They received intraperitoneal injections of 5%
565 dextrose in saline (2.5 ml) and their diet was supplemented with fruit and powder milk during the
566 following 2–3 days. After 3 days, animals behaved normally and were housed individually. Control
567 animals were injected with saline and received treatments similar to epileptic animals.

568 All experiments started after 6 weeks post-*status* and extended up to 25 weeks post-*status*, well into
569 the chronic epileptic phase. Seizures were observed in all animals during handling or recorded
570 electrophysiologically in a subset of animals. In some epileptic animals, we aimed to induce
571 convulsive seizures using high-pitched sounds (random pulses of 95-100 dB and 1-20 sec duration
572 at 0.05-1 Hz during 10 min). A convulsive motor seizure was defined according to clinical criteria,
573 as sustained and repeated forelimbs automatisms with or without falling. Control animals did never
574 exhibit convulsive seizures using this protocol.

575

576 *EEG recordings and analysis*

577 To evaluate epileptogenesis, some rats and mice were implanted with either intracranial 16-channel
578 silicon probes or skull EEG-grid of 32-channels (Neuronexus) under isoflurane anesthesia (1.5–2%
579 mixed in oxygen 400–800 ml/min). Jeweler's screws were inserted into the skull for providing
580 additional anchoring and reference/ground connections (over the cerebellum). The implant was
581 secured with dental cement. Animals were recovered from anesthesia and returned to home cages.

582 For recordings, EEG signals were pre-amplified (4x gain) and recorded with a 32-channel AC
583 amplifier (Axona), further amplified by 100, filtered by analog means at 1Hz to 5 kHz, and sampled
584 at 20 kHz/channel with 12 bits precision. EEG recordings were synchronized with a ceiling video
585 camera (30 frames/sec) to track the animal position in space.

586 Analysis of electrophysiological signals was implemented in MATLAB 9.3 (MathWorks). EEG
587 signals from the frontal and parietal electrodes were used to identify theta periods during running
588 (band-pass 4-12 Hz) and periods of immobility characterized by low frequency delta activity (0.5-
589 4Hz). Forward-backward-zero-phase finite impulse response (FIR) filters of order 512 were used
590 to preserve temporal relationships between channels and signals. Spectral values fitted to 1/f were
591 similar between groups for frequencies >150 Hz. HFO events were defined from the bandpass
592 filtered signal (80-120 Hz) by thresholding (>4 SDs). The power spectra were evaluated in a
593 window of ± 0.2 ms around each detected event. Time-frequency analysis was performed by
594 applying the multitaper spectral estimation in sliding windows with 97.7% overlap and frequency
595 resolution of 10 Hz in the 90-600 Hz frequency range. HFO activity was evaluated as the power
596 integral in the 80-120 Hz band.

597 We used a combination of features to identify HFO events automatically and to classify them in
598 different categories (*23*) (Supp.Fig.1). First we identified large amplitude transient (<100 ms)
599 discharges using LFP and current-source-density signals (CSD, i.e. the second spatial derivative)
600 at the SR and SLM. Second, we identified HFO events at the SP by frequency thresholding over
601 100 Hz. Then we used spectral indices such as entropy and fast ripple indices from candidate HFO
602 events at SP together with amplitude information from LFP and CSD signals at SR to classify events
603 as: a) SPW-ripples (low amplitude; 100-150 Hz); b) SPW-fast ripples (medium amplitude, >150
604 Hz) and IID-HFO (larger amplitude, >100 Hz). Events not meeting criteria were left unclassified.
605 Surface EEG recordings from mice were analyzed similarly, by using channels over the dorsal
606 hippocampus or at the frontal cortex to identify HFO events and channels over the parietal cortex
607 using selected segments of the EEG.

608

609 *In vivo recording and labeling of single cells*

610 Rats were anesthetized with urethane (1.2 g/kg, i.p.), fastened to the stereotaxic frame and warmed
611 to keep their body temperature at 37º. Two bilateral craniotomies of ~1 mm diameter were
612 performed for CA3 stimulation (AP: -1.2 mm, ML: 2.9 mm) and CA1 recordings (AP: -3.7 mm;
613 ML: 3 mm). The dura was gently removed, the *cisterna magna* was drained and the craniotomy
614 covered with warm agar to reinforce stability.

615 A 16-channel silicon probes (NeuroNexus Tech; 100 µm interspaced, 413 μm^2 contact) was
616 advanced perpendicular along the CA1-DG-CA3c axis guided by extracellular stimulation and
617 electrophysiological hallmarks. Extracellular signals were pre-amplified (4x gain) and recorded
618 with a 16(32)-channel AC amplifier (Multichannel Systems), further amplified by 100, analogically
619 filtered at 1Hz to 5 kHz, and sampled at 20 kHz/channel with 12 bits precision with a Digidata
620 1440. Concentric bipolar electrodes were advanced 3.5 mm with 30º in the coronal plane to
621 stimulate CA3. Stimulation consisted of biphasic square pulses (0.2 ms duration, 0.05-1.2 mA every
622 5 s). A subcutaneous Ag/AgCl wire in the neck served as reference. Recording and stimulus position
623 was confirmed by post hoc histological analysis.

624 Intracellular recording and labelling were obtained in current-clamp mode using sharp pipettes (1.5
625 mm/0.86 mm outer/inner diameter borosilicate glass; A-M Systems, Inc) were filled with 1.5 M
626 potassium acetate and 2% Neurobiotin (Vector Labs, Inc; 50-100 MΩ) (*59*). Signals were acquired

627 with an intracellular amplifier (Axoclamp 900A) at 100x gain. The resting potential, input
628 resistance and amplitude of action potentials was monitored all over the course of experiments.

629 After data collection, Neurobiotin was ejected using 500 ms depolarizing pulses at 1-3 nA at 1 Hz
630 for 10-45 min. Animals were perfused with 4% paraformaldehyde (PFA) and 15% saturated picric
631 acid in 0.1 M, pH 7.4 phosphate buffered saline (PBS). Brains were postfixed overnight at room
632 temperature (RT), washed in PBS and serially cut in 70 µm coronal sections (Leica VT 1000S
633 vibratome). Sections containing the stimulus and probe tracks were identified with a
634 stereomicroscope (S8APO, Leica). Sections containing Neurobiotin-labeled cells were localized by
635 incubating them in 1:400 Alexa Fluor 488-conjugated streptavidin (Jackson ImmunoResearch 016-
636 540-084) with 0.5% Triton X-100 in PBS (PBS-Tx) for 2 hours at room temperature (RT). To
637 evaluate morphological features of single cells, sections containing the somata of recorded cells
638 were processed with Triton 0.5% in PBS, blocked with 10% fetal bovine serum (FBS) in PBS-Tx
639 and incubated overnight at RT with the primary antibody solution containing rabbit anti-Calbindin
640 (1:500, CB D-28k, Swant CB-38) or mouse anti-Calbindin (1:1000, CB D-28k, Swant 300)
641 antibodies with 1% FBS in PBS-Tx. After three washes in PBS-Tx, sections were incubated for 2
642 hours at RT with appropriate secondary antibodies: goat anti-rabbit Alexa Fluor 633 (1:500,
643 Invitrogen, A21070), and goat anti-mouse Alexa Fluor488 (Jackson Immunoresearch, 115-545-
644 003) or goat anti-mouse Rhodamine Red (1:200, Jackson ImmunoResearch, 115-295-003) in PBS-
645 Tx-1% FBS. Following 10 min incubation with bisbenzimide H33258 (1:10000 in PBS, Sigma,
646 B2883) for nuclei labelling, sections were washed and mounted on glass slides in Mowiol (17%
647 polyvinyl alcohol 4-88, 33% glycerin and 2% thimerosal in PBS).

648 All morphological analyses were performed blindly to electrophysiological data. The distance from
649 the cell soma to radiatum was measured from confocal images using information from Calbindin
650 and bisbenzimide staining. All pyramidal cells included in this study were localized within the CA1
651 region. Calbindin immunostaining was used to estimate the width of the superficial sub-layer from
652 the border to the stratum radiatum. Superficial cells were defined based on the location of the soma
653 within the calbindin sublayer, independently on their immunoreactivity (*60*). The border with
654 radiatum was estimated for each section and the distance from the recorded cell somata was
655 measured using ImageJ (NIH Image).

656

657 *Analysis of intracellular single-cell recordings*

658 Analysis of electrophysiological data was performed using routines written in MATLAB 7.10
659 (MathWorks). Local field potential (LFP) recorded from sites at the stratum radiatum and
660 lacunosum moleculare were low-pass filtered at 100 Hz to identify sharp-waves and interictal
661 discharges using forward-backward-zero-phase finite impulse response (FIR) filters of order 512
662 to preserve temporal relationships between channels and signals. LFP signals from sites at the
663 stratum pyramidale were bandpass filtered between 100-600 Hz to study HFOs. For sharp-waves
664 and interictal discharges, filtered signals were smoothed by a Gaussian kernel and events were
665 detected by thresholding (>3 SDs). Interictal discharges were separated from sharp-waves by
666 amplitude and correlation across channels. For HFO detection, the bandpass-filtered signal was
667 subsequently smoothed using a Savitzky-Golay (polynomial) filter and events detected by
668 thresholding (>2 SDs) after artifact and noise rejection. All pairs of detected events were visually

669 confirmed and aligned by the peak of the accompanying sharp-wave and/or interictal discharge.
670 Time-frequency analysis of HFO events was performed by applying the multitaper spectral
671 estimation in sliding windows with 97.7% overlap and frequency resolution of 10 Hz in the 90-600
672 Hz frequency range (only the 100-600 Hz range is shown) to data sweeps aligned by sharp-wave
673 ripple events (± 1sec). Membrane potential responses of single-cells were evaluated in peri-event
674 plots before (-200 to -150 ms), during (±50 ms) and after (150 to 200 ms) HFO events.

675 Passive electrophysiological properties (input resistance, membrane decay and capacitance) of
676 neurons recorded intracellularly in vivo were measured using 500 ms currents step in current-clamp
677 mode. Cells with intracellular action potential amplitude smaller than 40 mV were excluded.
678 Resting membrane potential and input resistance were estimated by linear regression between
679 baseline potential data and the associated holding current. Intrinsic firing properties, including
680 action potential threshold, half-width duration and AHP were estimated from the first spike in
681 response to depolarizing current pulses of 0.2 nA amplitude and 500 ms duration. The sag and
682 maximal firing rate was calculated from current pulses of ±0.3 nA amplitude. A bursting index was
683 defined as the ratio of the number of complex spikes (minimum of 3 spikes <8 ms inter-spike
684 interval) over the total number of spikes recorded during theta activity.

685

686 *cFos immunostaining and analysis*

687 To evaluate immediate-early gene expression associated to sound-induced convulsive seizures,
688 animals were perfused 1 hour after and their brains cut in 70 µm coronal sections. Selected sections
689 were stained against c-Fos using a polyclonal antibody at 1:250 (Santa Cruz Biotechnology sC-52)
690 and bisbenzimide. Using one 20x confocal moisaic per animal, we quantified cFos intensity at CA1
691 pyramidal cells by delineating single-cell nuclei stained with bisbenzimide in one confocal plane
692 (ImageJ). The mean intensity of cFos signal from each cell was then normalized by subtracting the
693 background (set at 0) and dividing by the maximal positive signal in the mosaic, which was always
694 at granule cells (set at 1). No significant differences of background were observed across sections.
695 Delineated cells were ranked by their distance to radiatum to classify them as deep or superficial,
696 according to standard measurements of Calb1-layer thickness.

697

698 *Laser capture microdissection (LCM) and RNA isolation*

699 Brains from 3 control and 3 epileptic rats were dissected, longitudinally cut in half (separating both
700 hemispheres), wrapped in aluminum foil and immediately frozen in liquid nitrogen. To avoid
701 circadian effects on gene expression all samples were collected in the morning before noon and
702 conserved at -80ºC until use. The hippocampal region of each hemisphere was cut in 20µm slices
703 in a cryostat (Leica) (chamber temperature: -20ºC; block temperature: -30ºC) and placed on 1.0mm
704 PEN-membrane covered slides (Carl Zeiss). Slides were conserved at -20ºC until use. Right before
705 microdissection, slides were dried with vapor of liquid nitrogen. The CA1 cell layer was
706 microdissected with a Leica 6000 laser microdissector through a 40x non-oil immersion objective
707 to obtain cell bodies of superficial and deep sublayers separately (Fig.2A). Microdissected deep
708 and superficial areas were collected in different empty caps of 0.5ml Eppendorf tubes. After
709 microdissection, samples were processed following ARCTURUS PicoPure RNA Isolation Kit

710 (Thermo Fisher Scientific) instructions in order to extract and isolate total RNA. Briefly, 50µl of
711 extraction buffer was added into the cap, incubated at 42ºC for 30min, centrifuged at 800xG for
712 2min and stored at -80ºC. The same volume of 70% ethanol was added to the cell extract and the
713 mixture was pipetted into a pre-conditioned RNA purification column. The column was centrifuged
714 2min at 100xG and 30sec at 16000xG, and washed with 100µl of Wash Buffer 1. To completely
715 eliminate DNA, the purification column was treated with 40µl of DNAse (diluted 1/8 in RDD
716 Buffer) (Qiagen), incubated 15min and centrifuged at 8000xG for 15sec. Then the column was
717 washed twice with 100µl of Wash Buffer 2, and centrifuged at 8000xG after the first wash and at
718 16000xG after the second one. Finally, RNA was eluted into a new 0.5µl Eppendorf tube by adding
719 11µl of elution buffer onto the column membrane, incubating the column for 1min at room
720 temperature, and centrifuging the column for 1min at 1000xG and at 16000xG immediately after.
721 Total RNA samples were stored at -80ºC. RNA integrity number (RIN) was similar in control (4.7
722 ± 0.8) and epileptic rats (5.7 ± 0.5; P=0.07; 3 replicates x 2 sublayers per group), as well as for deep
723 (5.2 ± 0.9) and superficial sublayers (5.3 ± 0.1; P=0.81; n=6 replicates per sublayers).

724

725 *LCM-RNAseq library construction and sequencing*

726 RNA preparation for sequencing deep and superficial CA1 sublayers from control and epileptic rats
727 was performed as described in (*61*). The twelve samples were sequenced according to manufacturer
728 instructions in a HiSeq2500 sequencer (Illumina, Inc). Libraries were strand specific (reverse) and
729 sequenciation was performed in paired-end configuration with a read length of 75bp. Library size
730 of read pairs for the different samples analyzed was between 47 and 59 Million reads. RNAseq data
731 can be accessed at the GEO repository (GSE143555; reviewer token: ehitaysejlwdjad).

732

733 *LCM-RNAseq data analysis*

734 Alignment quality control of sequenced samples (LCM-RNAseq) was assessed with FastQC
735 (v.0.11.3) (Babraham Institute) and RNAseq tracks were visualized using IGV (v.2.3.57) (*62*).
736 LCM-RNAseq reads were mapped to the rat genome (Rnor_6.0.83) using STAR (v.2.5.0c) (*63*),
737 and files were further processed with Samtools (v.0.1.19). Aligned reads were counted to gene
738 transcripts using HTSeq (v.0.6.1) (*64*). Differential expression analysis was performed using
739 DESeq2 (v.1.10.0) (*65*) of the bioconductor suite (*66*) in the R (v.3.2.2) statistical computing
740 platform. The experimental design consisted in two factors (treatment and anatomical area) and
741 there was also grouped samples (samples from different anatomical areas (minus (deep) and plus
742 (superficial) that were obtained from individual mice). Genes were considered differentially
743 expressed at Benjamini-Hochberg (BH) Adj p-value<0.05 and absolute log2 fold change>0.3 (*67*),
744 except otherwise specified. GO analysis was performed using DAVID (v.6.8) bioinformatics
745 platform (*68*).

746

747 *LCM-RNAseq single-cell informed data analysis*

748 Single-cell RNAseq data from (*14*) was reanalyzed with consensus cluster SC3 algorithm (*69*).
749 From the original 3005 cells, pyramidal and interneurons were removed from somato-sensory

750 cortex, remaining 2442 cells. Remaining cells were reanalyzed downstream with SC3. Clustering
751 stability was optimal for 6 clusters. After that, one cluster presented high heterogeneity (mixed
752 population cluster), and was reanalyzed with the optimal clustering stability (5 clusters). Marker
753 genes were tested for every cluster with Wilcoxon signed rank test. Top 10 genes with the area
754 under the receiver operating characteristic (ROC) curve power >0.85 and with the Adj p-value<0.01
755 from both cluster analyses were selected, with a total of 69 bona-fide population markers. Based on
756 the markers, populations were fused/splitted and 3 populations were isolated in the first clustering
757 (pyramidal neurons, interneurons and oligodendrocytes) and 4 more in the second (astrocytes,
758 endothelial cells, microglia and mural cells). Sixteen outlier cells were removed by total_counts,
759 total_features or pct_counts_spike criteria, remaining 2,426 cells with a high correspondence with
760 the original classification: Astrocytes (155), Endothelial (177), Interneurons (174), Microglia (85),
761 Mural (56), Oligodendrocytes (804) and Pyramidal (975). To perform an informed analysis
762 leveraged on the subsetted and reanalized data from (*14*), the LCM-RNAseq was analyzed using
763 the 69 markers to identify genes that correlated with cell type. Furthermore, the relevant dimensions
764 (significant or top genes) from LCM-RNAseq data were used over the subsetted and the reanalized
765 dataset, to isolate the contribution of different cell-types across the control and epileptic conditions.

766

767 *Single-nuclei isolation*

768 We accurately isolated single nuclei from 2 control and 2 epileptic Calb1::CrexTdtomato young
769 adult mice. We used these animals to facilitate identification of the CA1 region under a fluorescent
770 scope. Animals were sacrificed 12 weeks after the kainate/saline administration by cervical
771 dislocation and brains were dissected and cut in 300um thick slices in a vibratome covered by ice
772 cold HBBS1x. As in LCM studies, samples were collected before noon to avoid circadian effects.
773 The dorsal CA1 region were manually dissected from 4 consecutive slices and put altogether into
774 400uL of ice-cold MACS buffer (0,5%BSA, 2mM EDTA, PBS1x). CA1 portions were transferred
775 to a dounce homogeneizer (20404 Lab Unlimited) containing 400uL of MACS buffer and were
776 homogeneized 12-15 times each with the pestle. The cell suspension was transferred to a 2mL
777 Eppendorf tube and centrifuge 15min 500G 4ºC. Cell pellets were resuspended in 500uL of lysis
778 buffer (10mM Tris-HCL, 10mM NaCl, 3mM MgCl2, 0,1% IGEPAL) and kept 5 minutes on ice.
779 Samples were then spun down at 500G for 30 min in a pre-chilled centrifuge. The nuclei pellet was
780 resuspended in PBS1x 1%BSA and then 15,000 nuclei were purified by flow cytometry in a BD
781 FACS Aria III. The whole process was carried out at 4º.

782

783 *Single-nucleus RNA sequencing*

784 Purified intact nuclei from mouse hippocampal CA1 area were processed through all steps to
785 generate stable cDNA libraries. For every sample, 15,000 nuclei were loaded into a Chromium
786 Single Cell A Chip (10x Genomics) and processed following the manufacturer's instructions.
787 Single-nuclei RNAseq libraries were prepared using the Chromium Single Cell 3' Library & Gel
788 Bead kit v2 and i7 Multiplex kit (10x Genomics). Pooled libraries were then loaded on a HiSeq2500
789 instrument (Illumina) and sequenced to obtain 75 bp paired-end reads following manufacturer
790 instructions. On sequencing depth, 262 million fragments were generated for the control condition

791 and 296 for the epileptic dataset. Libraries reached a sequencing saturation of 86.9% for control
792 and 91.2% for epilepsy condition. snRNAseq data can be accessed at the GEO repository
793 (GSE143560; reviewer token: gtkhqgegnjgldur).

794

795 *Single-nucleus RNA sequence analysis*

796 Quality control of sequenced reads was performed using FastQC (Babraham Institute). Sequenced
797 samples were processed using the Cell Ranger (v.2.2.0) pipeline (10x Genomics) and aligned to the
798 CRGm38 (mm10) mouse reference genome customized to count reads in introns (pre-mRNA) over
799 the Ensembl gene annotation version 94. Barcodes with total unique molecular identifier (UMI)
800 count >10% of the 99th percentile of the expected recovered cells were selected for further analysis.
801 Using this criterion, we retrieved 3,661 (control), 3,078 (epileptic) high quality nuclei per sample.
802 Mean reads per nucleus were 71,449 (control) and 96,150 (epileptic). Median genes per nucleus
803 were 71,449 (control) and 96,150 (epileptic). Minimum UMI count per nucleus were 710 (control),
804 540 (epileptic), well above the typical quality standards in single cell/nucleus sequencing. Single-
805 nucleus RNAseq data were subsequently pre-processed and further analysed in R (v.3.4.4) using
806 Seurat (v.2.3.4) (*70*, *71*). Filtering parameters were as follows: genes, nCell<5; cells, nGene<200.
807 Data were then normalized using global-scaling normalization (method: LogNormalize,
808 scale.factor=10.000). An initial exploratory analysis was performed on each dataset separately. This
809 analysis retrieved a similar number of clusters in each dataset that were approximately equal in size.
810 We next combine both datasets using the function MergeSeurat. Highly variable genes (HVGs)
811 were detected using FindVariableGenes function with default parameters. Then, normalized counts
812 on HVGs were scaled and centered using ScaleData function with default parameters. Principal
813 component analysis (PCA) was performed over the first ranked 1,000 HVGs, and cluster detection
814 was carried out with Louvain algorithm in FindClusters function, using 20 first PCA dimensions
815 and resolution of 0.6 (the default number in Seurat and the optimal according to cell number, data
816 dispersion and co-expression of previously reported cell markers). Plots of the two principal
817 components of the PCA where cells were colored by dataset of origin excluded the presence of
818 batch effects. This analysis identified 13 clusters. CA1 pyramidal neurons populated three of these
819 clusters: one cluster was enriched in bona fide gene markers of deep cells (*Ndst4*, *Coll11a1*)
820 whereas a second one was enriched in canonical markers of superficial cells (*Calb1*, *Epha3*). The
821 third cluster showed a mixed identity. An additional round of clustering segmented this population
822 in three additional clusters that were enriched in deep and superficial markers, respectively, and a
823 third cluster that could not be annotated based on the presence of gene markers of CA1 sublayer
824 neurons. The vast majority of cells within this cluster (66/67) were from epileptic mice (Pyr_ES).
825 Next, the FindMarkers function was used to identify gene markers and to determine the cell
826 populations represented by each cluster. Finally, cell subtypes were manually aggregated based on
827 the presence of canonical markers of known cell types into six distinct major cell types: excitatory
828 neurons (Excit); inhibitory neurons (Inter); oligodendrocytes (ODC); oligodendrocyte progenitor
829 cells (OPCs); microglia (Microglia); astrocytes (Astro). Visualization and embedding were
830 performed using stochastic nearest neighbors (tSNE) (*72*) and uniform manifold approximation and
831 projection (UMAP) (*73*)methods over PCA using the 20 first PCA dimensions. UMAP plots of
832 gene expression show normalized count (UMIs) per nucleus. The equalized expression between

833 fixed percentiles was plotted according to the following criteria: the minimum expression was
834 adjusted to 5% and the maximum expression was adjusted to 95% in all UMAP expression plots.
835 To evaluate effects of epilepsy, datasets from both conditions were merged and HVGs were
836 identified for each dataset as above indicated. Only HVGs that were detected in all datasets were
837 used to perform visualization and embedding as described above. Clustering was performed on
838 merged dataset from both conditions and populations were identified combining these results with
839 clustering information obtained in control and epileptic datasets separately, together with co-
840 expression of population markers. Differential expression analysis (DEA) was used to identify
841 population gene markers. For DEA, the nuclei of each population were contrasted against all the
842 other nuclei in the merged dataset using Wilcoxon Rank Sum test on normalized counts. For
843 epilepsy effect analysis, in the merged dataset, the nuclei of each population from the epileptic
844 dataset were contrasted against all the other nuclei of the same population in control using Wilcoxon
845 Rank Sum test on normalized counts. GO functional enrichment analyses were performed using
846 DAVID (v.6.8) bioinformatics platform (*68*).

847

848 *Cell trajectories and pseudotime analysis*

849 The disease pseudotime analysis was performed using Monocle 2 (v.2.8.0) (*42*). First, the Seurat
850 merged dataset was transformed to Monocle object and cells from Pyr_CA1 were subset. The size
851 factor and dispersion of the subset was estimated, and data was normalized and preprocessed. Genes
852 under the minimum level detection threshold of 0.1 and detected in less than 10 cells were filtered
853 with the function setOrderingFilter. Genes defining how a cell progress through a pseudo-time
854 disease trajectory were selected with the function differentialGeneTest (Monocle's main differential
855 analysis routine). 2579 genes (64,68% of a total of 3987 genes considered as expressed) were
856 significative with FDR<1% for the combination of factors: ~SeuratCluster+Condition, and thus,
857 defined the high dimensional space for pseudotemporal trajectory analysis. Discriminative
858 dimensionality reduction with trees (DDRTree) reduction algorithm learns the principal graph and
859 specifies the trajectory. DDRTree was applied inside the function reduceDimension, and got the
860 default parameters: norm_method = "log", pseudo_expr = 1, relative_expr = TRUE,
861 auto_param_selection = TRUE (automatically calculate the proper value for the ncenter (number
862 of centroids)) and scaling = TRUE (scale each gene before running trajectory reconstruction). Prior
863 the dimensional reduction, the function reduceDimension also performed a variance-stabilization
864 of the data (because the expressionFamily of the data was negbinomial.size). Finally, the cells were
865 ordered according to pseudo-time with the function orderCells, which added a pseudo-time value
866 and state for each cell; together encode where each cell maps to the trajectory. For enrichment
867 analysis on pseudotime trajectories, top-ranked 250 branched expression analysis modeling
868 (BEAM) significant changes through the progression across the disease trajectory for each sublayer
869 were clusterized and GO enrichment analyses on upregulated and downregulated clusters were
870 performed using DAVID (v.6.8) bioinformatics platform (*68*).
871

872 *Cell-type immunostaining and analysis*

873 To evaluate the contribution of different cell-types, control and epileptic rats and mice were
874 perfused with 4% paraformaldehyde (PFA) and 15% saturated picric acid in 0.1 M PBS, pH 7.4.
875 Brains were postfixed overnight and cut in 70 µm coronal sections (Leica VT 1000S vibratome).
876 Sections containing the dorsal-intermediate hippocampus were processed with Triton 0.5% in PBS
877 and blocked with 10% fetal bovine serum (FBS) in PBS-Tx. Sections were incubated overnight at
878 RT with 1% FBS PBS-Tx solution containing primary antibodies against a battery of cell-type
879 specific markers. The list of antibodies include: rabbit anti-calbindin (1:1000, CB D-28k, Swant
880 CB-38) or mouse anti-calbindin (1:500, CB D-28k, Swant 300) to identify superficial CA1
881 pyramidal cells; rabbit anti-Wfs1 (1:500, Protein Tech, 11558-1-AP) for CA1 pyramidal cells;
882 rabbit anti-Iba1 (1:1000, Wako, 019-19741) for microglia; rabbit anti-GFAP (1:1000, Sigma,
883 G9269) for astrocytes; rabbit anti-Olig2 (1:200, Millipore, AB9610) for oligodendrocytes. After
884 three washes in PBS-Tx, sections were incubated for 2 hours at RT with appropriate secondary
885 antibodies: goat anti-rabbit Alexa Fluor633 (1:200, ThermoFisher, A-21070), and donkey anti-
886 mouse Alexa Fluor488 (1:200, ThermoFisher, A-21202) or goat anti-mouse Rhodamine Red
887 (1:200, Jackson ImmunoResearch, 115-295-003) in PBS-Tx-1%FBS. Following 10 min incubation
888 with bisbenzimide H33258 (1:10000 in PBS, Sigma, B2883) for nuclei labelling, sections were
889 washed and mounted on glass slides in Mowiol (17% polyvinyl alcohol 4-88, 33% glycerin and 2%
890 thimerosal in PBS).

891 To acquire multichannel fluorescence stacks from recorded cells, a confocal microscope (Leica
892 SP5) with LAS AF software v2.6.0 build 7266 (Leica) was used. For single-cell studies the
893 following channels (fluorophore, laser and excitation wavelength, emission spectral filter) were
894 used: a) bisbenzimide, Diode 405 nm, 415–485 nm; b) Alexa Fluor 488, Argon 488 nm, 499–535
895 nm; c) Rhodamine Red / Alexa Fluor 568 / Texas Red, DPSS 561nm, 571–620 nm; d) Alexa Fluor
896 633, HeNe 633 nm, 652–738 nm; and objectives HC PL APO CS 10.0x0.40 DRY UV, HCX PL
897 APO lambda blue 20.0x0.70 IMM UV and HCX PL APO CS 40.0x1.25 OIL UV were used.

898

899 *FluoroJade staining*

900 To evaluate neurodegenerating neurons we used coronal sections from epileptic rats perfused at
901 different time points post-*status* (from 2 to 3 weeks). Selected sections were immunostained against
902 Wfs1 followed by FluoroJade staining. To this purpose, sections were pretreated for 5 min with 1%
903 sodium hydroxide in 80% ethanol, followed by 70% ethanol (2 min) and distilled water (2min).
904 Sections were then incubated 10 min in 0.06% potassium permanganate, rinsed in distilled water
905 and immersed into 0.0001% solution of FluoroJade C dye (Sigma AG325) in 0.1% acetic acid (pH
906 3.5) for 10min. After a brief wash in distilled water, they were mounted on gelatin-coated slides,
907 air-dried, coverslipped with DPX and examined under a confocal microscope as described above.
908 FluoroJade positive cells exhibited bright green fluorescence.
909

910 *In situ hybridization analysis*

911 Selected sections from control and epileptic rats were processed for in situ hybridization using
912 standard methods. Briefly, riboprobes were prepared from Rat *Enpp2* cDNA (Image clone ID
913 7115236) and using RT-PCR from rat adult hippocampus to prepare *Wfs1* (NM_031823.1, from bp
914 783 to 1631), *Ndst4* (XM_006233274.2, from bp 536 to 1024), *Syt17* (NM_138849.1, from bp 378
915 to 1118), *Hrt1a* (J05276.1, from bp 730 to 1663) and *Scn7a* (NM_131912.1, from bp 2812 to 3550)
916 cDNAs. Similar riboprobes were used in sections from normal and epileptic mice. Riboprobe
917 hybridization was detected using alkaline phosphatase–coupled anti-digoxigenin Fab fragments
918 (Sigma). Hybridized sections were mounted in glycerol and photographed using a Nikon
919 stereoscope and a DCC Nikon camera.

920

921 *RNAscope analysis*

922 Control and epileptic mice were perfused with 4% paraformaldehyde (PFA) and 15% saturated
923 picric acid in 0.1 M PBS, pH 7.4. Brains were post-fixed overnight and cut in 50 µm coronal
924 sections (Leica VT 1000S vibratome). Sections containing the dorsal-intermediate hippocampus
925 were mounted onto SuperFrost Plus microscope slides (10149870, ThermoFisher Scientific).
926 RNAscope Fluorescent Multiplex Assay (Advanced Cell Diagnostics) was carried out according to
927 the manufacturer's protocols. Briefly, sections were dehydrated at 60ºC, follow by ethanol,
928 pretreated with a target retrieval solution (322000, ACD) and protease III (322340, ACD), and co-
929 hybridized with Spag5 (Mm-Spag5, 505691, ACD) and Dcc (Mm-Dcc-C3, 427491, ACD) probes.
930 Finally, the amplification steps (RNAscope Fluorescent Multiplex Detection reagents, 320851,
931 ACD) were followed, using Atto 550 for Spag5 and Atto 647 for Dcc as fluorescent labels. The
932 RNAscope 3-plex positive control probe set (320881, ACD), with probes to Polr2a, PPIB and UBC,
933 was used to confirm preservation of sample RNA. The negative control probe to bacterial DapB
934 (320871) was used to establish non-specific labelling.

935 Following the RNAscope protocol, sections were blocked for 30 min with 10% FBS in PBS-Tx,
936 and incubated overnight at RT with rabbit anti-Wfs1 (1:500, Protein Tech, 11558-1-AP) in 1% FBS
937 PBS-Tx. After three washes in PBS, sections were incubated for 2 h with donkey anti-rabbit Alexa
938 Fluor488 (1:200, ThermoFisher Scientific, A-21206) in 1% FBS PBS-Tx, washed twice in PBS and
939 mounted using ProLong Gold Antifade mountant (ThermoFisher Scientific, P10144).

940 Multichannel fluorescence stacks were achieved in a confocal microscope (Leica SP5) with LAS
941 AF software v2.6.0 build 7266 (Leica), with a 40x objective (HCX PL APO CS 40.0x1.25 OIL
942 UV), at 1 µm z-interval. Following lasers (excitation wavelength, emission spectral filter) were
943 used for each fluorophore: Argon (488 nm, 499–535 nm) for Alexa Fluor488, DPSS (561nm, 571–
944 620 nm) for Atto 550, and HeNe (633 nm, 652–738 nm) for Atto 647. Diode (405 nm, 415–485
945 nm) was used as an unstained channel to identify autofluorescent material, which can be abundant
946 in epileptic tissue.

947 To estimate the amount of *Spag5* and *Dcc* transcripts, we calculated the number of dots per cell
948 using ImageJ (Fiji). In one confocal plane per image, we counted single signal dots, in either Dcc
949 or Spag5 channels, in each ROI. ROIs were drawn as the outline of several pyramidal cell somas,
950 based on their Wfs1 immunoreactivity. Only those which were focus at their centre in the selected

951 plane were drawn. When we found clusters instead of individual dots, we converted intensity to dot
952 number as suggested by the manufacturer (ACD): (total intensity -average background intensity x
953 area)/single dot average intensity.

954

955 *Statistical analysis*

956 Statistical analysis was performed with MATLAB, SPPSS and using the computing environment
957 R (R Development Core Team, 2005). No statistical method was used to predetermine sample sizes.
958 Normality and homoscedasticity were evaluated with the Kolmogorov–Smirnov and Levene's tests,
959 respectively. The exact number of replications for each experiment is detailed in text and figures.
960 Several ways ANOVAs or Kruskal-Wallis tests were applied. Post hoc comparisons were evaluated
961 with the Tukey-Kramer, Student or Wilcoxon tests. Deep-superficial trends were evaluated using
962 Spearman correlation and tested against 0 (i.e., no correlation was the null hypothesis) at $p<0.05$
963 (two sided).

964

965 *Data and code availability*

966 Two open R Shiny applications provide visualization of LCM-RNAseq
967 (http://lopezatalayalab.in.umh-csic.es/CA1_Sublayers_&_Epilepsy/) and snRNAseq
968 (http://lopezatalayalab.in.umh-csic.es/CA1_SingleNuclei_&_Epilepsy/) data.
969

Supplementary Materials

Supplementary tables are included in MS Office Excel format as follows:

Table S1: Electrophysiological properties of deep and superficial cells.

Table S2: LCM-RNAseq data.

Table S3: snRNAseq data.

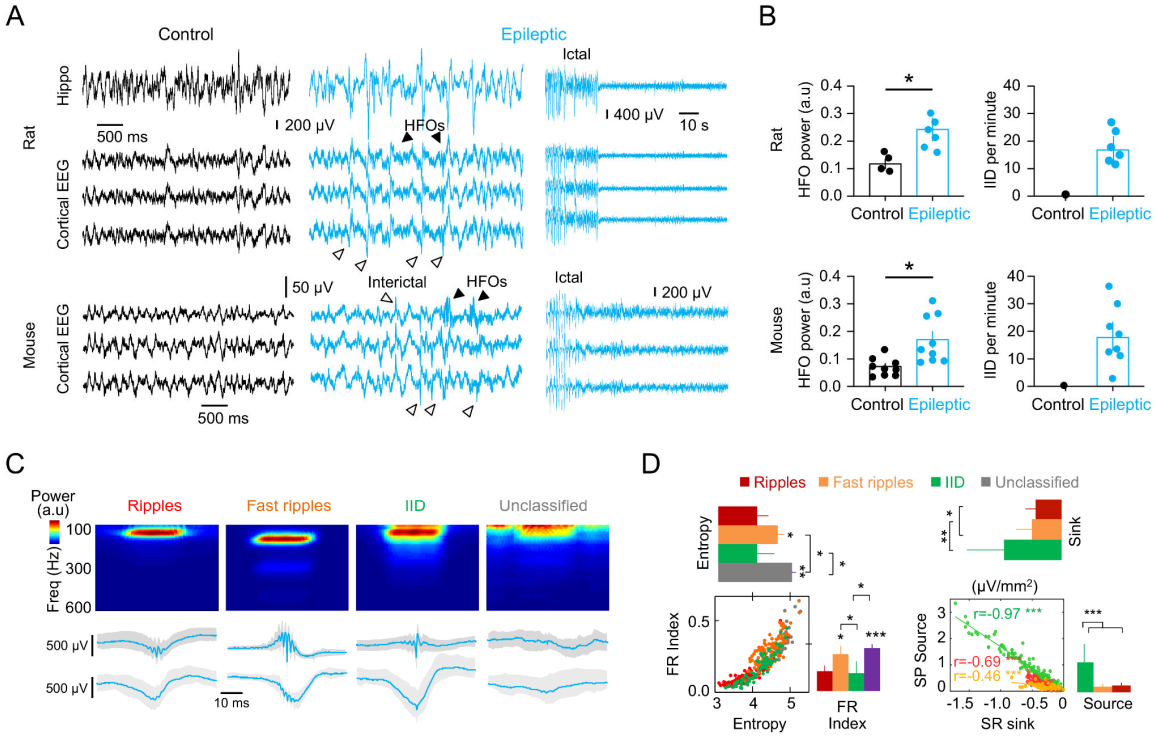

Fig.S1. Electrophysiological analysis. A, Cortical EEG and/or intrahippocampal recordings from epileptic rats and mice allowed evaluation of neurophysiological changes accompanying acquired epilepsy. Simultaneous cortical and hippocampal recordings are shown for rats, while cortical EEG is shown for mice. Note interictal discharges (IID) and high-frequency oscillations (HFOs) in epileptic animals recorded both intracranially and at the cortical surface over the hippocampus. The small size of the mouse brain and connectivity between the hippocampus and prefrontal cortex facilitates recording of HFOs at scalp. The late stage of a seizure recorded in both animals is shown to highlight ictal activity. **B**, Quantification of the HFO power and IID rate in rats and mice 6 weeks after status. IID rate was evaluated from 20 min sessions in epileptic animals. Data from 1 session from 6 rats and 3 sessions from 3 mice. *, $p<0.05$ unpaired t-test. **C**, Sharp-wave (SPW) associated HFO events recorded from the dorsal hippocampus of urethane anesthetized epileptic rats were automatically detected and separated as ripples (100-150 Hz), fast ripples (>150 Hz) and IID using amplitude and spectral information. Some events were left unclassified. **D**, Quantitative separation of ripples, fast ripples and IID events. Spectral indices such as entropy and fast ripple indices were combined with information on the amplitude of current-source density (CSD) signals. IID were clearly separated from SPW events using CSD amplitude of sinks and sources. Asterisks reflect significant differences from post hoc Tuckey tests as *, $p<0.05$; **, $p<0.01$ and ***, $p<0.001$.

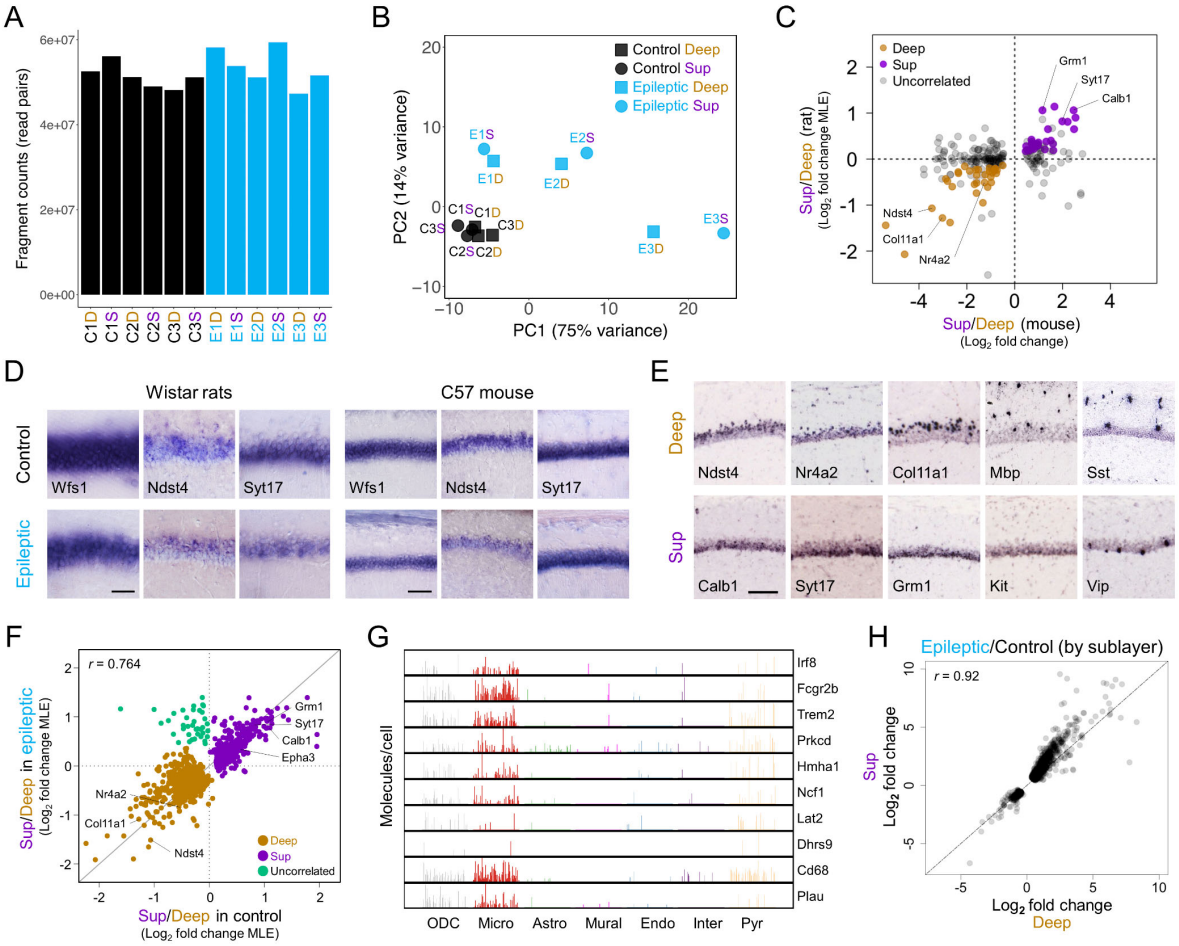

Fig.S2. CA1 sublayer-specific gene expression profiling from bulk tissue (LCM-RNAseq). A, Bar graph showing per-sample sequencing depth. Note similar library size of about $50*10^6$ fragments per sample in both groups (paired-end sequencing). **B**, Principal component analysis of normalized rlog counts. Note pairwise clustering of deep and superficial samples from the same animals and significant separation between control and epileptic replicates, suggesting that transcriptional variability successfully captures between-group differences. **C**, Scatterplot showing differentially expressed genes (false discovery ratio, FDR<0.1) between superficial and deep manually sorted neurons from mice (x-axis; data from Cembrowski et al., 2016) against change in mRNA expression for these genes in our bulk-tissue LCM-RNAseq data from rats (y-axis). Colored points indicate genes that were differentially expressed across sublayers in both species. **D**, ISH of the pan-CA1-specific marker *Wfs1*, the superficial sublayer marker *Syt17* and deep sublayer marker *Ndst4* in representative hippocampal sections from control and epileptic rats and mice. Note sublayer markers are not all-or-none, but rather reflect a gradient distribution. Scale bar, 100 µm. **E**, Allen Brain Atlas (ABA) ISH sections showing additional genes differentially regulated in deep and superficial sublayers in mouse. Note regionalization of some interneuron-specific genes such as Sst and Vip, as well as non-neuronal genes such as Mbp. Scale bar, 100 µm. **F**, Scatter plot of DEGs in superficial and deep CA1 sublayers from control and epileptic rats (Adj p-val<0.05). Most transcripts are highly correlated, except for a subset of transcripts (green). **G**, Bar plot of the eleven

1012 cell-type-specific uncorrelated DEGs from F suggest contribution of different cell-type populations,
1013 especially microglia. **H**, Scatter plot showing changes in gene expression upon epilepsy in CA1
1014 superficial and deep sublayer. Plot includes all differentially expressed genes in epilepsy (global
1015 effect: 732 unregulated, 185 downregulated genes (Adj p-val<0.01 and LFC>0.5).
1016

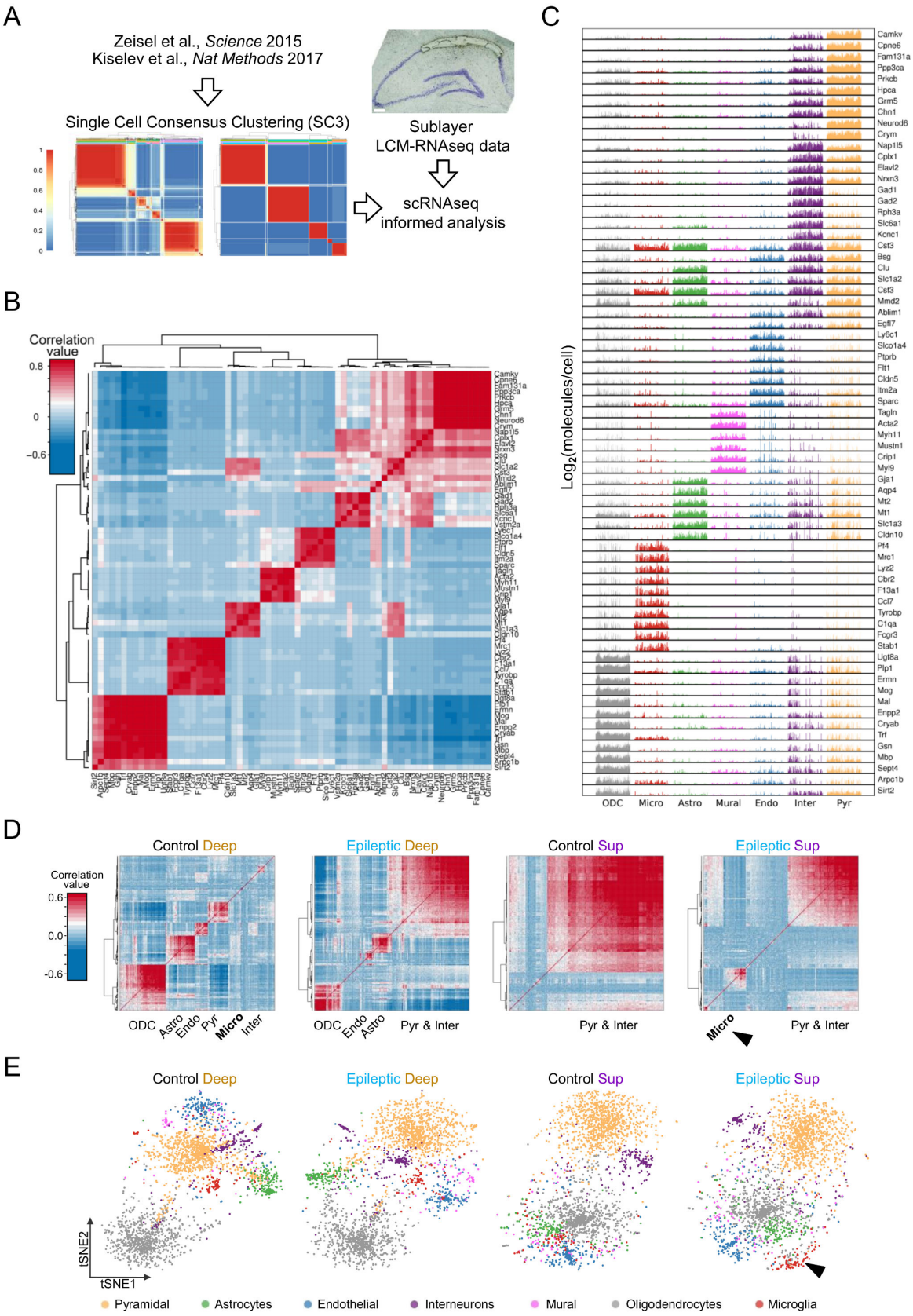
A
Zeisel et al., Science 2015
Kiselev et al., Nat Methods 2017
Single Cell Consensus Clustering (SC3)
Sublayer
LCM-RNAseq data
scRNAseq
informed analysis
B
Correlation value
0.8
0
−0.6
C
Log2(molecules/cell)
ODC
Micro
Astro
Mural
Endo
Inter
Pyr
D
Control Deep
Epileptic Deep
Control Sup
Epileptic Sup
Correlation value
0.6
0.0
-0.6
ODC
Astro
Endo
Pyr
Micro
Inter
Pyr & Inter
E
tSNE2
tSNE1
Pyramidal
Astrocytes
Endothelial
Interneurons
Mural
Oligodendrocytes
Microglia

1017

1018 **Fig.S3. Single-cell informed analysis of LCM-RNAseq data from bulk hippocampal CA1**
1019 **tissue. A**, Workflow analytic steps to identify cell-type heterogeneity in CA1 hippocampal area
1020 from bulk tissue RNAseq data. Single-cell consensus clustering (SC3) analysis (Kiselev et al.,
1021 2017) was performed on previously published single-cell RNAseq data from mouse cortex and
1022 hippocampus (Zeisel et al., 2015) to identify major gene markers of cell types in CA1 area. Next,
1023 snRNAseq data for genes identified in LCM-RNAseq analyses (gene lists of top differentially
1024 expressed genes between CA1 sublayers of control and epileptic rats) was used to identify the
1025 presence of cell type gene markers and co-expressed genes at single cell level. **B**, A list of 69 cell-
1026 type gene markers was obtained using SC3 on single-cell RNAseq data from Zeisel et al. (2015).
1027 **C,** Bar plot showing expression levels as log2(molecules/cell) of the 69 cell type gene markers at
1028 single cell level (x-axis) across the seven major cell types identified. Pyr, pyramidal neurons; Inter,
1029 interneurons; ODC, oligodendrocytes; Astro, astrocytes; Endo, endothelial cells; Micro, microglia;
1030 Mural, mural cells. **D**, Clustered correlation matrices of expression levels of differentially expressed
1031 genes between deep and superficial CA1 sublayers from control and epileptic rats. Sets of
1032 differentially expressed genes of the same size (top 250 DEG) were used to investigate cell type
1033 heterogeneity in each condition. Note distinct cell-types segregate across sublayers. Note also larger
1034 number of microglial transcripts in response to epilepsy in superficial sublayer (arrowhead). **E**, t-
1035 Distributed Stochastic Neighbor Embedding (t-SNE) maps were generated using scRNAseq data
1036 for genes identified as differentially expressed between deep and superficial CA1 sublayers from
1037 control and epileptic rats. Sets of differentially expressed genes (top 250 DEG) were used to
1038 investigate cell type heterogeneity in each condition (max. Adj p-val = 0.029).

A

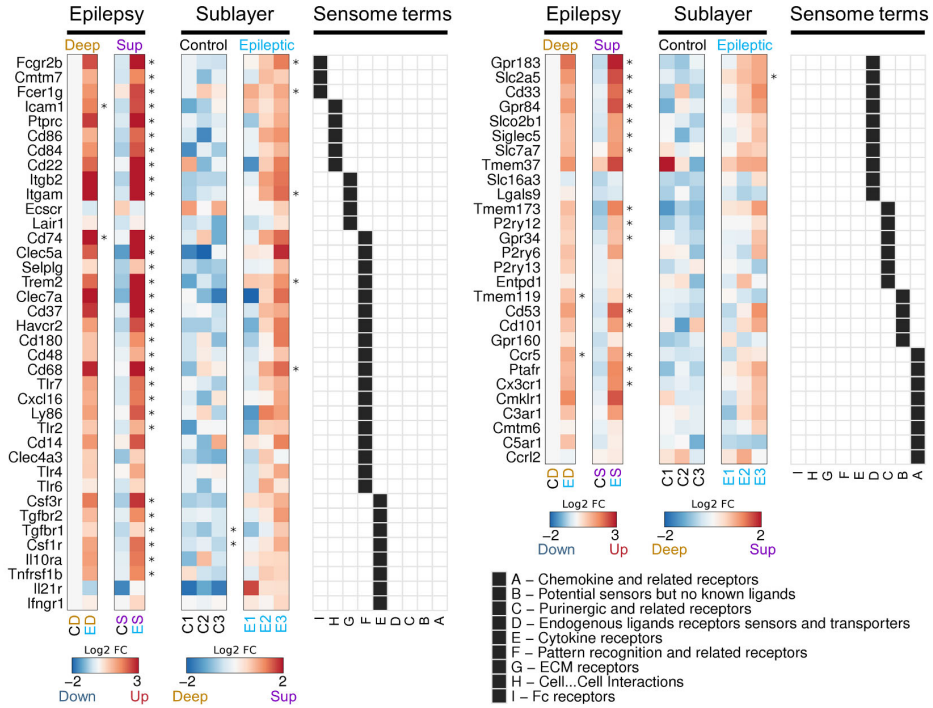

B

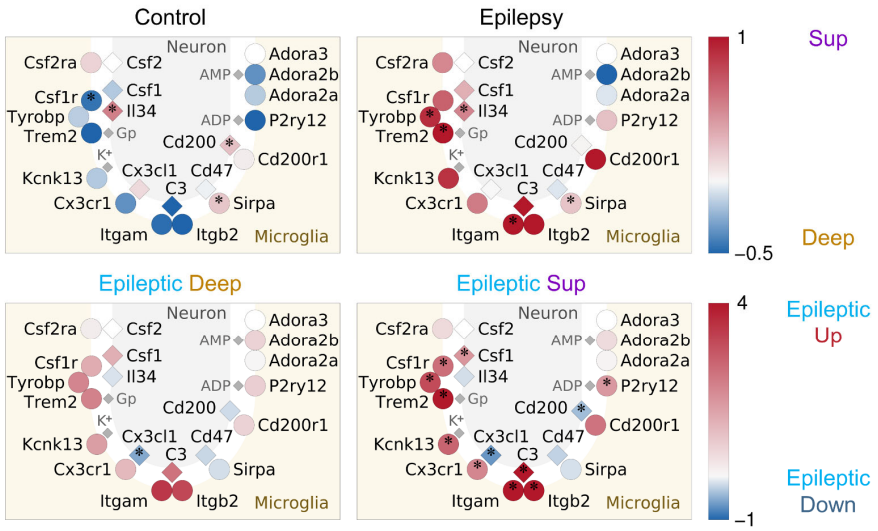

Fig.S4. Transcriptional changes associated with microglia in the epileptic CA1 (bulk tissue LCM-RNAseq). A, Heatmaps of log2 fold changes for genes annotated to the microglial sensome (Hickman et al., 2013). Log2 fold change values are for the epilepsy effect in superficial and deep sublayers (Epilepsy), and for sublayer effect in control and epileptic mice (Sublayer). * Adj p-value<0.1. Gene Ontology annotation (GO BP) is shown at the foremost right (black squares). The list continues from left to right. **B**, Schematic diagram illustrating neuron-glia interactions via ligand-receptor pairings. Neuronal ligands (diamonds) and microglia receptors (circles) are colored

1046 by expression fold change (see color scheme legend) in the comparison between superficial and
1047 deep sublayer in control (top-left) and epileptic (top-right) CA1, and for epilepsy effect in deep
1048 (bottom-left) and superficial (bottom-right) CA1 sublayer. * Adj p-value<0.1.
1049

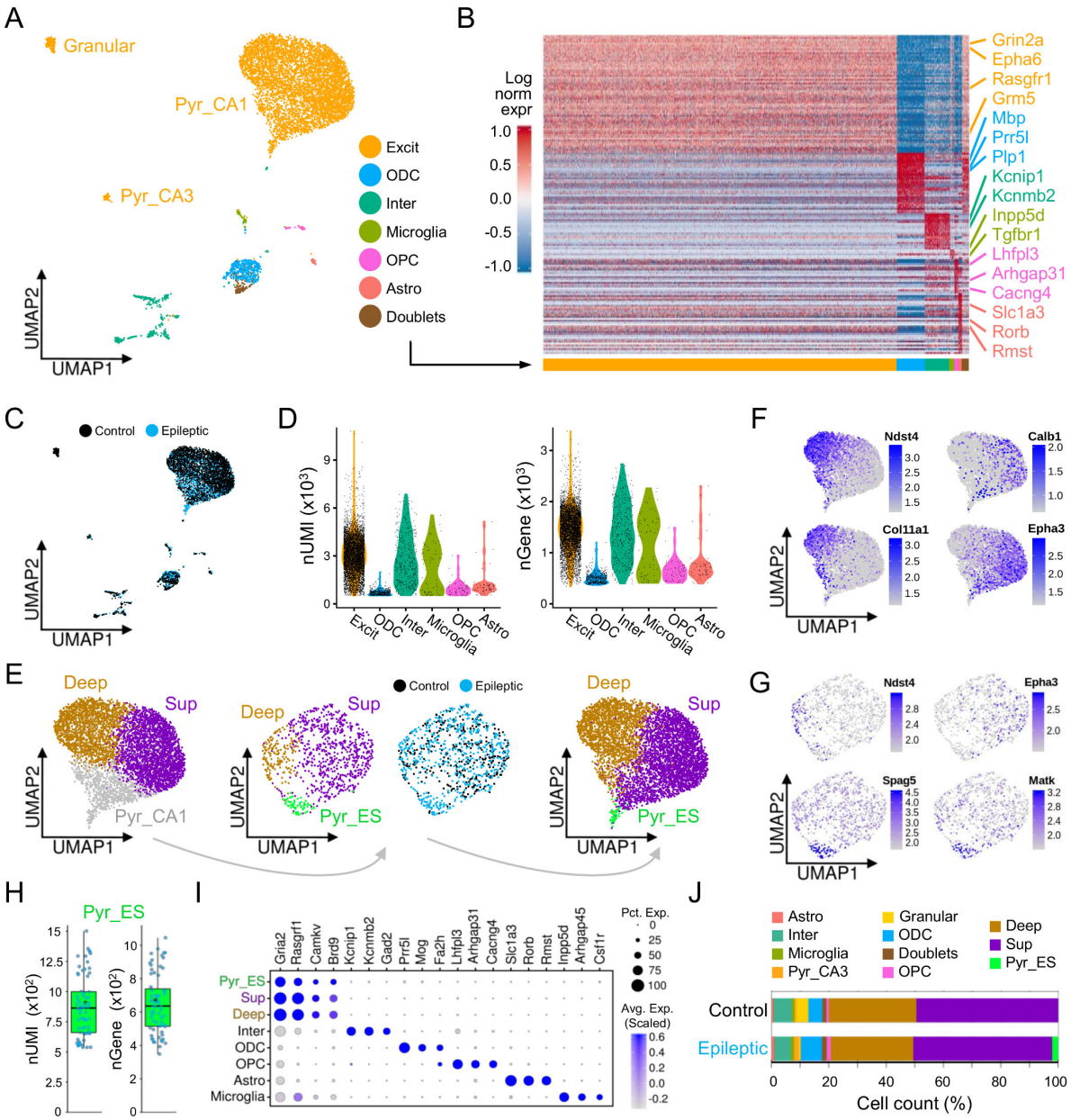

Fig.S5. Transcriptional profiling at single-nucleus level unfolds heterogeneity of excitatory pyramidal neurons in the basal and epileptic hippocampal CA1 area. A, Uniform Manifold Approximation and Projection (UMAP) plot from snRNAseq transcriptional profiling showing 6 major cell classes identified and annotated in our CA1 samples. **B**, Heatmap of cell-type marker genes (168 enriched genes with AUC power>= 0.55) expression per single-nucleus across identified cell populations. **C,** UMAP plot of the snRNAseq datasets split by condition. **D**, Violin plots showing distribution of nUMI (left) and nGene (right) per major populations as indicated in the legend. **E**, UMAP clustering of the CA1 pyramidal cell population took two rounds. In the first round, nuclei were automatically separated in three main subclusters: deep cells, superficial cells and a third cluster of pyramidal neurons (Pyr_CA1). In the second round, the subsetted Pyr_CA1 cells were sorted as deep and superficial and epilepsy-specific Pyr_ES cells (green). **F**, UMAP of

1061 the pyramidal cell class colored by normalized expression levels for the indicated subpopulation
1062 gene markers. **G**, UMAP of the subsetted pyr_CA1 pyramidal cells. Note separation of deep and
1063 superficial cells, as well as the epilepsy-specific pyramidal cell subpopulation (Pyr_ES). **H**, Box
1064 plots showing nUMI (left) and nGene (right) per cell in the epilepsy-specific population Pyr_ES
1065 population. **I**, Confirmation of cell-type specific gene mapping of sorted cells. **J**, Proportions of the
1066 distinct cell types and populations identified across conditions (control and epilepsy). Note the
1067 epilepsy-specific population Pyr_ES (light green).
1068

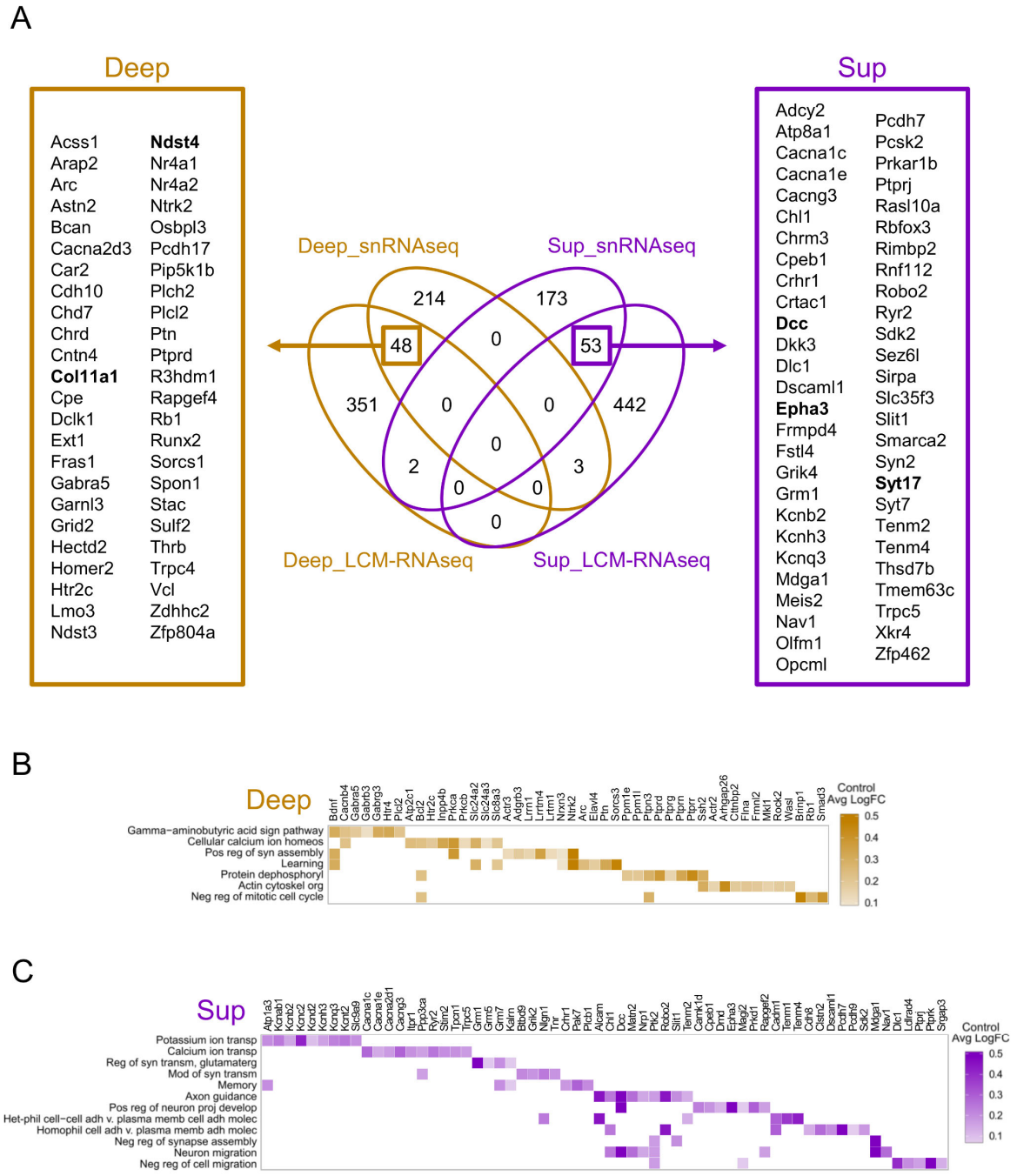

Fig.S6. Equivalence between LCM-RNAseq and snRNAseq sublayer-specific results. A, Venn diagram showing overlap in genes identified as significantly enriched in superficial (Sup_LCM_RNAseq) and deep sublayer (Deep_LCM-RNAseq) by bulk CA1 sublayer-specific tissue gene expression profiling (LCM-RNAseq) or snRNAseq. Many sublayer- and cell-subtype significantly enriched transcripts were common across species (rat, mouse) and technologies (bulk RNAseq, snRNAseq). **B**, Functional GO analysis of genes significantly enriched in deep (top) or superficial (bottom) CA1 neurons (snRNAseq) in the control animals.

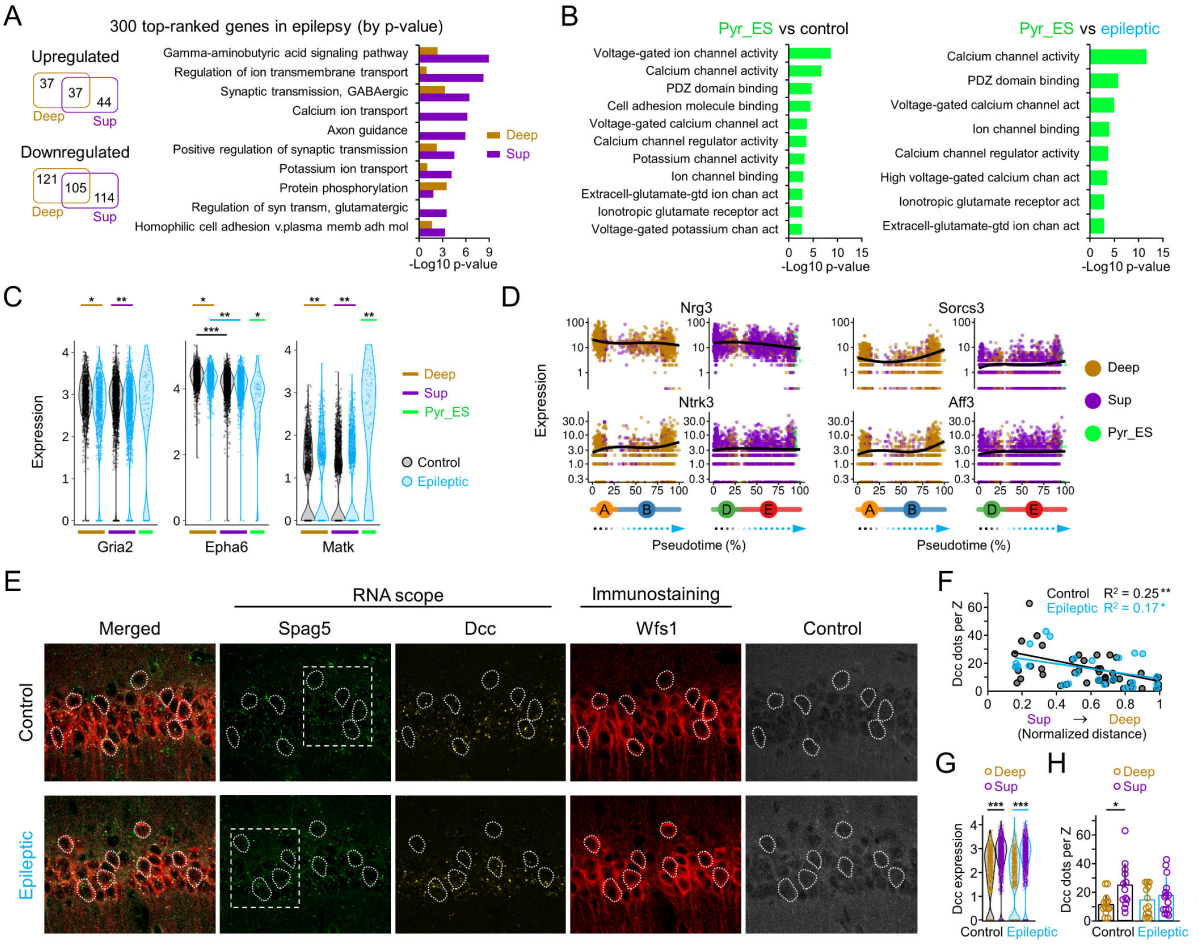

Fig.S7. Gene profiling at single cell nuclei reveals transcriptional changes in superficial and deep CA1 neurons in experimental epilepsy. A, Venn diagram and Go terms of top-ranked 300 genes modulated by epilepsy. **B**, Bar chart of significance (left) and fold change (right) for most upregulated genes in Pyr_ES when compared with epileptic CA1 pyramidal cells (absolute fold change >0.5 and transcript detection in >50% of the nuclei). **C,** Violin plots showing normalized expression value (normalized log transformed UMIs) by condition (control, black; epilepsy, blue) and population (deep, occher; superficial, purple; Pyr_ES, lightgreen) of selected gene markers of pyramidal neurons (*Gria2*, *Epha6*), and *Knain2* which is modulated by epilepsy in superficial and deep cells. Note specific upregulation in Pyr_ES cells. *p<0.05; **p<1E-10; ***p<1E-50 (Wilcoxon rank sum test). **D**, Examples of gradient progression across disease trajectory for significantly modulated genes in epilepsy related to neuronal survival (*Nrg3*, *Ntrk3*, *Sorcs3*, *Aff3*). **E**, Combined RNAscope and immunostaining analysis allowed identification of cells with extreme expression of *Spag5* in situ. Neurons having their soma cut transversally by the confocal plane are outlined. Discontinuous line boxes identify the region expanded in Fig.5. The channel Control (405 nm) was used to control for autofluorescent signals across channels, which are characteristic of epileptic tissue (labeled Control at the rightmost). **F**, Distribution of *Dcc* dots per cells along their normalized position in the deep-superficial axis. Note similar trends for control and epileptic cells (significant Pearson correlation). **G**, Violin plot for *Dcc* gene (normalized log transformed UMIs)

in nuclei of CA1 superficial (Sup) and deep (Deep) pyramidal cells from control (black) and epileptic (blue) animals. ***p<1E-50 (Wilcoxon rank sum test). **H**, Quantification of *Dcc* signals in deep and superficial CA1 pyramidal cells as counted in one confocal plane from 3 control and 3 epileptic mice (2-way ANOVA effect for sublayer F(1, 51)=6.771, p =0.012; no group differences nor interaction). Data from 27 control (14 deep, 14 superficial) and 28 epileptic cells (15 deep, 13 superficial).

References and Notes

1. Z. Chen, M. J. Brodie, D. Liew, P. Kwan, Treatment Outcomes in Patients With Newly Diagnosed Epilepsy Treated With Established and New Antiepileptic Drugs: A 30-Year Longitudinal Cohort Study. *JAMA Neurol.* **75**, 279–286 (2018).
2. I. Blümcke *et al.*, International consensus classification of hippocampal sclerosis in temporal lobe epilepsy: a Task Force report from the ILAE Commission on Diagnostic Methods. *Epilepsia*. **54**, 1315–29 (2013).
3. F. Du, T. Eid, E. W. Lothman, C. Köhler, R. Schwarcz, Preferential neuronal loss in layer III of the medial entorhinal cortex in rat models of temporal lobe epilepsy. *J. Neurosci.* **15**, 6301–13 (1995).
4. N. C. de Lanerolle *et al.*, A retrospective analysis of hippocampal pathology in human temporal lobe epilepsy: evidence for distinctive patient subcategories. *Epilepsia*. **44**, 677–87 (2003).
5. I. Blümcke *et al.*, Towards a clinico-pathological classification of granule cell dispersion in human mesial temporal lobe epilepsies. *Acta Neuropathol.* **117**, 535–44 (2009).
6. K. G. Davies *et al.*, Relationship of hippocampal sclerosis to duration and age of onset of epilepsy, and childhood febrile seizures in temporal lobectomy patients. *Epilepsy Res.* **24**, 119–26 (1996).
7. A. R. Wyler, F. Curtis Dohan, J. B. Schweitzer, A. D. Berry, A grading system for mesial temporal pathology (hippocampal sclerosis) from anterior temporal lobectomy. *J. Epilepsy*. **5**, 220–225 (1992).
8. M. Morin-Brureau *et al.*, Microglial phenotypes in the human epileptic temporal lobe. *Brain*. **141**, 3343–3360 (2018).
9. R. Coras *et al.*, Differential influence of hippocampal subfields to memory formation: insights from patients with temporal lobe epilepsy. *Brain*. **137**, 1945–57 (2014).
10. G. R. Rodrigues *et al.*, Increased frequency of hippocampal sclerosis ILAE type 2 in patients with mesial temporal lobe epilepsy with normal episodic memory. *Brain*. **138**, e359 (2015).
11. S. Saghafi *et al.*, Histopathologic subtype of hippocampal sclerosis and episodic memory performance before and after temporal lobectomy for epilepsy. *Epilepsia*. **59**, 825–833 (2018).
12. A. Prada Jardim *et al.*, Characterising subtypes of hippocampal sclerosis and reorganization: correlation with pre and postoperative memory deficit. *Brain Pathol.* **28**, 143–154 (2018).
13. G. W. Mathern, P. A. Kuhlman, D. Mendoza, J. K. Pretorius, Human fascia dentata anatomy and hippocampal neuron densities differ depending on the epileptic syndrome and age at first seizure. *J. Neuropathol. Exp. Neurol.* **56**, 199–212 (1997).
14. A. Zeisel *et al.*, Cell types in the mouse cortex and hippocampus revealed by single-cell RNA-seq. *Science (80-.)*. **347**, 1138–1142 (2015).
15. N. Habib *et al.*, Div-Seq: Single-nucleus RNA-Seq reveals dynamics of rare adult newborn

1143 neurons. *Science (80-.).* **353**, 925–928 (2016).
1144 16. H.-W. Dong, L. W. Swanson, L. Chen, M. S. Fanselow, A. W. Toga, Genomic-anatomic
1145 evidence for distinct functional domains in hippocampal field CA1. *Proc. Natl. Acad. Sci.*
1146 *U. S. A.* **106**, 11794–9 (2009).
1147 17. M. S. Cembrowski *et al.*, Spatial Gene-Expression Gradients Underlie Prominent
1148 Heterogeneity of CA1 Pyramidal Neurons. *Neuron*. **89**, 351–68 (2016).
1149 18. L. Slomianka, I. Amrein, I. Knuesel, J. C. Sørensen, D. P. Wolfer, Hippocampal pyramidal
1150 cells: The reemergence of cortical lamination. *Brain Struct. Funct.* **216** (2011), pp. 301–
1151 317.
1152 19. M. Valero, L. M. de la Prida, The hippocampus in depth: a sublayer-specific perspective of
1153 entorhinal–hippocampal function. *Curr. Opin. Neurobiol.* **52**, 107–114 (2018).
1154 20. I. Soltesz, A. Losonczy, CA1 pyramidal cell diversity enabling parallel information
1155 processing in the hippocampus. *Nat. Neurosci.* **21**, 484–493 (2018).
1156 21. L. Wittner *et al.*, Synaptic reorganization of calbindin-positive neurons in the human
1157 hippocampal CA1 region in temporal lobe epilepsy. *Neuroscience*. **115**, 961–978 (2002).
1158 22. M. E. Morris, K. G. Baimbridge, H. el-Beheiry, G. V Obrocea, A. S. Rosen, Correlation of
1159 anoxic neuronal responses and calbindin-D28k localization in stratum pyramidale of rat
1160 hippocampus. *Hippocampus*. **5**, 25–39 (1995).
1161 23. M. Valero *et al.*, Mechanisms for Selective Single-Cell Reactivation during Offline Sharp-
1162 Wave Ripples and Their Distortion by Fast Ripples. *Neuron*. **94**, 1234-1247.e7 (2017).
1163 24. J. G. R. Jefferys *et al.*, Mechanisms of physiological and epileptic HFO generation. *Prog.*
1164 *Neurobiol.* **98** (2012), pp. 250–264.
1165 25. M. Thom *et al.*, Variability of sclerosis along the longitudinal hippocampal axis in
1166 epilepsy: A post mortem study. *Epilepsy Res.* **102**, 45–59 (2012).
1167 26. M. S. Cembrowski, L. Wang, K. Sugino, B. C. Shields, N. Spruston, Hipposeq: a
1168 comprehensive RNA-seq database of gene expression in hippocampal principal neurons.
1169 *Elife*. **5**, e14997 (2016).
1170 27. K. D. Winden, A. Bragin, J. Engel, D. H. Geschwind, Molecular alterations in areas
1171 generating fast ripples in an animal model of temporal lobe epilepsy. *Neurobiol. Dis.* **78**,
1172 35–44 (2015).
1173 28. S. E. Hickman *et al.*, The microglial sensome revealed by direct RNA sequencing. *Nat.*
1174 *Neurosci.* **16**, 1896–905 (2013).
1175 29. R. H. Hoek *et al.*, Down-regulation of the macrophage lineage through interaction with
1176 OX2 (CD200). *Science (80-.).* **290**, 1768–1771 (2000).
1177 30. K. Biber, H. Neumann, K. Inoue, H. W. G. M. Boddeke, Neuronal "On" and "Off" signals
1178 control microglia. *Trends Neurosci.* **30** (2007), pp. 596–602.
1179 31. J. Luo *et al.*, Colony-stimulating factor 1 receptor (CSF1R) signaling in injured neurons
1180 facilitates protection and survival. *J. Exp. Med.* **210**, 157–172 (2013).
1181 32. M. Inostroza *et al.*, Hippocampal-Dependent spatial memory in the water maze is
1182 preserved in an experimental model of temporal lobe epilepsy in rats. *PLoS One*. **6** (2011).
1183 33. J. C. You *et al.*, Epigenetic suppression of hippocampal calbindin-D28k by ΔfosB drives
1184 seizure-related cognitive deficits. *Nat. Med.* **23**, 1377–1383 (2017).
1185 34. A. M. Iacopino, S. Christakos, Specific reduction of calcium-binding protein (28-kilodalton
1186 calbindin-D) gene expression in aging and neurodegenerative diseases. *Proc. Natl. Acad.*
1187 *Sci. U. S. A.* **87**, 4078–4082 (1990).
1188 35. G. Curia, D. Longo, G. Biagini, R. S. G. Jones, M. Avoli, The pilocarpine model of
1189 temporal lobe epilepsy. *J. Neurosci. Methods*. **172**, 143–57 (2008).
1190 36. S. Bialik, A. Kimchi, The Death-Associated Protein Kinases: Structure, Function, and
1191 Beyond. *Annu. Rev. Biochem.* **75**, 189–210 (2006).
1192 37. U. Pfisterer, K. Khodosevich, Neuronal survival in the brain: Neuron type-specific

1193 mechanisms. *Cell Death Dis.* **8** (2017), pp. e2643–e2643.
1194 38. E. J. Huang, L. F. Reichardt, Neurotrophins: Roles in Neuronal Development and Function.
1195 *Annu. Rev. Neurosci.* **24**, 677–736 (2001).
1196 39. J. He, A. R. Green, Y. Li, S. Y. T. Chan, D. X. Liu, SPAG5: An Emerging Oncogene.
1197 *Trends in Cancer* (2020), , doi:10.1016/j.trecan.2020.03.006.
1198 40. J. Katic, G. Loers, J. Tosic, M. Schachner, R. Kleene, The cell adhesion molecule CHL1
1199 interacts with patched-1 to regulate apoptosis during postnatal cerebellar development. *J.*
1200 *Cell Sci.* **130**, 2606–2619 (2017).
1201 41. H. Tawarayama *et al.*, Draxin regulates hippocampal neurogenesis in the postnatal dentate
1202 gyrus by inhibiting DCC-induced apoptosis. *Sci. Rep.* **8** (2018), doi:10.1038/s41598-018-
1203 19346-6.
1204 42. X. Qiu *et al.*, Reversed graph embedding resolves complex single-cell trajectories. *Nat.*
1205 *Methods*. **14**, 979–982 (2017).
1206 43. X. Qiu *et al.*, Single-cell mRNA quantification and differential analysis with Census. *Nat.*
1207 *Methods*. **14**, 309–315 (2017).
1208 44. M. Valero *et al.*, Determinants of different deep and superficial CA1 pyramidal cell
1209 dynamics during sharp-wave ripples. *Nat. Neurosci.* **18**, 1281–1290 (2015).
1210 45. A. V Masurkar *et al.*, Medial and Lateral Entorhinal Cortex Differentially Excite Deep
1211 versus Superficial CA1 Pyramidal Neurons. *Cell Rep.* **18**, 148–160 (2017).
1212 46. F. Laurent *et al.*, Proximodistal structure of theta coordination in the dorsal hippocampus
1213 of epileptic rats. *J. Neurosci.* **35**, 4760–75 (2015).
1214 47. M. Maroso *et al.*, Cannabinoid Control of Learning and Memory through HCN Channels.
1215 *Neuron*. **89**, 1059–73 (2016).
1216 48. I. Ali, D. Chugh, C. T. Ekdahl, Role of fractalkine-CX3CR1 pathway in seizure-induced
1217 microglial activation, neurodegeneration, and neuroblast production in the adult rat brain.
1218 *Neurobiol. Dis.* **74**, 194–203 (2015).
1219 49. U. B. Eyo *et al.*, Neuronal hyperactivity recruits microglial processes via neuronal NMDA
1220 receptors and microglial P2Y12 receptors after status epilepticus. *J. Neurosci.* **34**, 10528–
1221 10540 (2014).
1222 50. A. Vezzani, T. Z. Baram, New Roles for Interleukin-1 Beta in the Mechanisms of Epilepsy.
1223 *Epilepsy Curr.* **7**, 45–50 (2007).
1224 51. O. K. Steinlein, J. L. Noebels, Ion channels and epilepsy in man and mouse. *Curr. Opin.*
1225 *Genet. Dev.* **10**, 286–91 (2000).
1226 52. A. B. Dixit *et al.*, RNA-seq analysis of hippocampal tissues reveals novel candidate genes
1227 for drug refractory epilepsy in patients with MTLE-HS. *Genomics*. **107**, 178–188 (2016).
1228 53. O. Peñagarikano *et al.*, Absence of CNTNAP2 leads to epilepsy, neuronal migration
1229 abnormalities, and core autism-related deficits. *Cell*. **147**, 235–246 (2011).
1230 54. K. Kanekura *et al.*, A Rac1/phosphatidylinositol 3-kinase/Akt3 anti-apoptotic pathway,
1231 triggered by alsinLF, the product of the ALS2 gene, antagonizes Cu/Zn-superoxide
1232 dismutase (SOD1) mutant-induced motoneuronal cell death. *J. Biol. Chem.* **280**, 4532–
1233 4543 (2005).
1234 55. N. M. Ashpole, A. Hudmon, Excitotoxic neuroprotection and vulnerability with CaMKII
1235 inhibition. *Mol. Cell. Neurosci.* **46**, 720–730 (2011).
1236 56. R. S. Vest, H. O'Leary, S. J. Coultrap, M. S. Kindy, K. U. Bayer, Effective post-insult
1237 neuroprotection by a novel Ca2+/ calmodulin-dependent protein kinase II (CaMKII)
1238 inhibitor. *J. Biol. Chem.* **285**, 20675–20682 (2010).
1239 57. N. A. Bishop, T. Lu, B. A. Yankner, Neural mechanisms of ageing and cognitive decline.
1240 *Nature*. **464** (2010), pp. 529–535.
1241 58. G. N. Patrick *et al.*, Conversion of p35 to p25 deregulates Cdk5 activity and promotes
1242 neurodegeneration. *Nature*. **402**, 615–622 (1999).

59. E. Cid, L. M. de la Prida, Methods for single-cell recording and labeling in vivo. *J. Neurosci. Methods*. **325** (2019), , doi:10.1016/j.jneumeth.2019.108354.
60. M. Valero *et al.*, Determinants of different deep and superficial CA1 pyramidal cell dynamics during sharp-wave ripples. *Nat. Neurosci.* **18** (2015), doi:10.1038/nn.4074.
61. M. Scandaglia *et al.*, Loss of Kdm5c Causes Spurious Transcription and Prevents the Fine-Tuning of Activity-Regulated Enhancers in Neurons. *Cell Rep*. **21**, 47–59 (2017).
62. H. Thorvaldsdóttir, J. T. Robinson, J. P. Mesirov, Integrative Genomics Viewer (IGV): High-performance genomics data visualization and exploration. *Brief. Bioinform.* **14**, 178–192 (2013).
63. A. Dobin *et al.*, STAR: Ultrafast universal RNA-seq aligner. *Bioinformatics*. **29**, 15–21 (2013).
64. S. Anders, P. T. Pyl, W. Huber, HTSeq-A Python framework to work with high-throughput sequencing data. *Bioinformatics*. **31**, 166–169 (2015).
65. M. I. Love, W. Huber, S. Anders, Moderated estimation of fold change and dispersion for RNA-seq data with DESeq2. *Genome Biol.* **15** (2014), doi:10.1186/s13059-014-0550-8.
66. W. Huber *et al.*, Orchestrating high-throughput genomic analysis with Bioconductor. *Nat. Methods*. **12**, 115–121 (2015).
67. Y. Benjamini, Y. Hochberg, Controlling the False Discovery Rate: A Practical and Powerful Approach to Multiple Testing. *J. R. Stat. Soc. Ser. B*. **57**, 289–300 (1995).
68. D. W. Huang, B. T. Sherman, R. A. Lempicki, Systematic and integrative analysis of large gene lists using DAVID bioinformatics resources. *Nat. Protoc.* **4**, 44–57 (2009).
69. V. Y. Kiselev *et al.*, SC3: Consensus clustering of single-cell RNA-seq data. *Nat. Methods*. **14**, 483–486 (2017).
70. A. Butler, P. Hoffman, P. Smibert, E. Papalexi, R. Satija, Integrating single-cell transcriptomic data across different conditions, technologies, and species. *Nat. Biotechnol.* **36**, 411–420 (2018).
71. T. Stuart *et al.*, Comprehensive Integration of Single-Cell Data. *Cell*. **177**, 1888-1902.e21 (2019).
72. L. van der Maaten, G. Hinton, Visualizing Data using t-SNE. *J. Mach. Learn. Res.* **9**, 2579–2605 (2009).
73. L. McInnes, J. Healy, J. Melville, UMAP: Uniform Manifold Approximation and Projection for Dimension Reduction (2018) (available at http://arxiv.org/abs/1802.03426).

Acknowledgments

General: We thank Beatriz Lázaro, Ester Lara, Laura Dolón and Juan Moriano for technical help.

Funding: Supported by grants from the Spanish Ministerio de Economía y Competitividad (MINECO) to LMP (RTI2018-098581-B-I00), Fundación Tatiana Pérez de Guzman el Bueno and the Thematic Research Network SynCogDis (SAF2014-52624-REDT and SAF2017-90664-REDT). JLA was supported by grants from the Spanish Ministry of Science, Innovation and Universities co-financed by ERDF (RYC-2015-18056 and RTI2018-102260-B-I00) and Severo Ochoa Grant SEV-2017-0723. RRV and ABayes were supported by grants from MINECO BFU2015-69717-P and RTI2018-097037-B-100, The Marie Curie Career Integration Grant (ref. 304111) and the Thematic Research Network SynCogDis (SAF2014-52624-REDT and SAF2017-90664-REDT). AVM was supported by the Spanish Ministerio de Economía y Competitividad (SAF2017-85717-R) and Fundación Alicia Koplowitz. AB was supported by grants SAF2017-

87928-R from MICINN co-financed by ERDF and RGP0039/2017 from the Human Frontiers Science Program Organization (HFSPO). The Instituto de Neurociencias is a “Centre of Excellence Severo Ochoa”. DGD and CMN hold a PhD fellowships from the Spanish Ministry of Economy and Competitiveness (BES-2013-064171, BES-2016-076281).

Author contributions: LMP, JPLA, ABayes and ABarco designed the study. LMP and JPLA coordinated experiments and analysis. EC, MV, BG, DM, CMN, LBE, RRV, AVM, LD, IFL and DGD obtained data. YH and MS provided the Thy1.2-G-CaMP7-T2A-DsRed2 mouse line. EC, AMG, MV, BG, AB, JPLA and LMP analyzed and interpreted the data. AMG developed online tools. LMP and JPLA drafted the paper. All authors commented and contributed.

Competing interests: There are no competing interests.

Data and materials availability: Two open R Shiny applications provide visualization of LCM-RNAseq (http://lopezatalayalab.in.umh-csic.es/CA1_Sublayers_&_Epilepsy/) and snRNAseq (http://lopezatalayalab.in.umh-csic.es/CA1_SingleNuclei_&_Epilepsy/) data.